Chemical Engineering and Processing 97 (2015) 213–232

Contents lists available at ScienceDirect

Chemical Engineering and Processing: Process Intensification

journal homepage: www.elsevier.com/locate/cep

Computational fluid dynamics modeling of mixing effects for crystallization in coaxial nozzles

Carl Pirkle Jr.[a,b], Lucas C. Foguth[b], Steven J. Brenek[c], Kevin Girard[c], Richard D. Braatz[b,*]

[a] Department of Chemical and Biomolecular Engineering, University of Illinois at Urbana-Champaign, United States
[b] Department of Chemical Engineering, Massachusetts Institute of Technology, United States
[c] Pfizer Global Research & Development, Eastern Point Road, Groton, CT 06340, United States

ARTICLE INFO

Article history:
Received 7 May 2015
Received in revised form 1 July 2015
Accepted 3 July 2015
Available online 16 July 2015

Keywords:
Micromixers
Static mixers
Coaxial mixers
Crystallization
Computational fluid dynamics
Population balance models

ABSTRACT

A leading method for the crystallization of pharmaceutical compounds is to rapidly mix an antisolvent with a solvent saturated with the desired drug. Compared to cross-flow mixers, coaxial nozzles have negligible buildup of crystalline material on their surfaces and are less likely to plug. Rather than requiring moving parts, the inlet velocities of the input solvent and antisolvent streams provide the necessary mechanical energy for turbulent mixing. Computational fluid dynamics (CFD), micromixing modeling, and the population balance equation (PBE) are coupled in the simulation of coaxial nozzle crystallization of lovastatin-saturated methanol by intense mixing with the antisolvent water. The simulations show that flow rates of inlet streams have a profound effect on crystal size distribution (CSD), which is caused by different degrees of inhomogeneity in the supersaturation and nucleation and growth rates. Other important process parameters are pipe length of pipe downstream of the injection point and the inner and outer pipe diameters. To the authors' knowledge, this is the most detailed simulation study on coaxial crystallizers reported to date. The simulation results show the feasibility of tailoring a specific crystal size distribution by adjusting the operating conditions (such as inlet stream velocities) of the coaxial crystallizer.

1. Introduction

Pharmaceutical crystals should be optimally sized to dissolve at the proper therapeutic rate. More specifically, controlling the crystal size distribution (CSD) is necessary to meet product specifications, such as bioavailability, and to ensure the efficiency of downstream processes (e.g., filtration and drying) [1–3]. Otherwise, additional processes such as milling and granulation are required [4–5].

Antisolvent crystallization refers to addition of a miscible "antisolvent" to the solvent saturated with the desired solute. Since the solubility of the solute in the antisolvent is very low, supersaturation is quickly induced, creating a driving force for crystallization. An advantage of using antisolvent crystallization is its ability to induce the crystallization of thermally sensitive pharmaceuticals without large temperature variations [6–7]. However, this method requires rapid and sufficient mixing of the antisolvent with the solute dissolved in solvent, which, in turn, necessitates the design of an appropriate mixer/crystallizer to accomplish intense mixing and crystallization on a fine scale.

Several different types of antisolvent mixers have been used for crystallization. State-of-the-art crystallization units, such as coaxial mixer/crystallizers (Fig. 1), utilize high intensity mixing of the antisolvent and the solution to produce crystals smaller than 25 μm, which improves the bioavailability and increases the dissolution rate of the final drug product [1–3]. The ability to obtain such small crystals can also allow the elimination of undesirable unit operations such as milling [4–5]. Agitated semibatch mixers/crystallizers [38] and impinging jet mixers/crystallizers [9] are two additional types of crystallizers commonly used in industry.

Many crystallizer designs have been explored to generate high supersaturation in such mixtures as an approach for generating consistent crystal nuclei that are subsequently grown to a desired size [3,10–14]. Compared to cross-flow mixers, coaxial jet mixers have negligible buildup of crystalline material on their surfaces and are less likely to plug. Coaxial mixers can be designed to deliver rapid turbulent mixing using short sections of pipe. As the energy required for mixing is provided by the inlet streams, with no moving metal parts and no bearings, these devices have simple maintenance and operation. Some experimental and modeling

* Corresponding author. Fax: +1 617 258 5042.
E-mail address: braatz@mit.edu (R.D. Braatz).

http://dx.doi.org/10.1016/j.cep.2015.07.006
0255-2701/

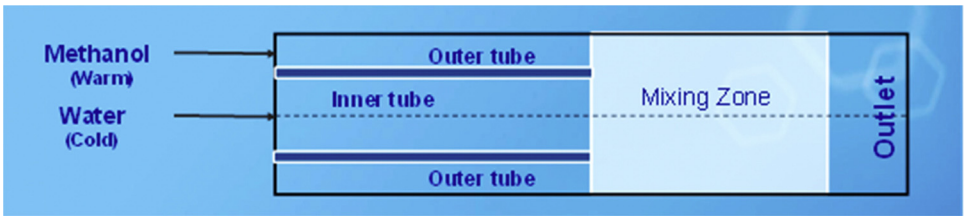

Fig. 1. Diagram of coaxial nozzle used as a mixer/crystallizer (courtesy of Parkaj Doshi).

studies of coaxial crystallizers have been published to gain deeper understanding and to facilitate more efficient development and optimization of the coaxial mixer crystallization process [15–18].

Various experimental studies of antisolvent crystallization in an agitated semibatch vessel indicate that the crystal size distribution (CSD) depends strongly on operating conditions such as agitation rate, mode of addition (direct or reverse), addition rate, solvent composition, and size of the crystallizer [3,19–25,26–31]. The polymorphic or pseudopolymorphic form can also depend on the operating conditions [32–37].

The number of operating conditions that can be investigated is large, so that investigating these combinations by bench-scale experiments can be time consuming and costly. This development time and cost can be reduced by using computer simulation to augment the experimental approach to mixer/crystallizer investigation and design. This article considers important design parameters for crystallization in coaxial mixers: the length of pipe downstream of the injection point, the velocity and temperature of the inlet streams, and the inner and outer pipe diameters.

Computer simulation is used throughout industry to gain understanding and guidance in development of manufacturing processes. These simulation problems usually involve large systems of algebraic equations (AEs) and ordinary and partial differential equations (ODEs, PDEs). In the case of pharmaceutical crystallization, a meaningful description of the process requires PDE/AEs over a multiscale spatial domain. For a dynamic model, the independent variables consist of time (t), spatial location (X–Y–Z) within the crystallizer, and geometric variables for the crystal, such as a characteristic size r. In addition, some critical transport processes occur at a subgrid, or sub-cellular level, which can be handled without increasing the number of independent variables through use of probability density functions.

This article describes an effort whose goal is to speed up the design of the coaxial crystallizers to tailor the crystal size distribution according to the bioavailability and drug administration requirements. Dynamic simulations of a confirmed coaxial crystallizer were carried out that simultaneously solve partial differential equations for macromixing, micromixing, and a population balance for the crystals. The computational model [38–40] was used, which replaces a quadrature-method-of-moments model used to simulate the time evolution of the particle size distribution by Rodney Fox [41] with a full spatially varying population balance model implemented using a high resolution finite-volume method. This article employs an extension of the model [38–40] to include temperature effects on the crystallization. Our simulations were used to perform a parameter sensitivity analysis (see Varma et al. [42] for background on such analyses) to identify the key model parameters and to simulate variations in their values on the full crystal size distribution (CSD) in the antisolvent crystallization of lovastatin, using kinetics reported in the literature [43]. The effects of inlet concentrations and stream flow rates on CSD were numerically investigated and compared with CSDs obtained in a dual-impinging jet crystallizer [40]. As observed in simulations of dual impinging jets, the mean crystal size and the width of the distribution are found to decrease with an increase in inlet stream velocity. The simulation results show different degrees of inhomogeneity in the supersaturation and the nucleation and growth rates for different inlet stream flow rates.

2. Model equations

2.1. Multi-scale modeling

A multi-scale system of algebraic and partial differential equations is solved in order to simulate a pharmaceutical crystallizer. For a dynamic system, time (t) is one of the independent variables, which will range from 0 to a value sufficiently large to approximate steady state. The axial and transverse coordinates X–Y–Z represent the location in the mixer/crystallizer. For an axisymmetric mixer such as the coaxial mixer, a two-dimensional X–Y grid can be used to lower computational cost. Although modeling the turbulent macromixing processes requires the use of only these spatial coordinates and time as independent variables, a higher resolution of the flow field is required to model the interactions between hydrodynamics, nucleation, and growth. An additional geometric independent variable is also introduced, which is associated with the crystal size represented by a single characteristic dimension r.

The approach used here couples a turbulent computational fluid dynamic (CFD) code with a multienvironment probability density (PDF) model, which captures the micromixing in the subgrid scale, and the population balance equation (PBE), which models the evolution of the crystal size distribution.

2.2. Macro-mixing equations (CFD code)

Turbulent transport of mass, momentum, and energy is discussed thoroughly in Pope's definitive textbook [44]. The Fluent User's Manual summarizes the relevant equations, and Fluent 13 was used to obtain solutions to these equations [45]. The version of Fluent used for the calculations presented in this paper is included in Ansys 14.5 [46]. In general form, the equations are:

$$\text{Continuity equation}: \frac{\partial \rho}{\partial t} + \nabla\cdot(\rho v) = 0 \tag{1}$$

Momentum conservation equation :

$$\frac{\partial}{\partial t}(\rho \boldsymbol{v}) + \nabla\cdot(\rho \boldsymbol{v}\boldsymbol{v}) = -\nabla p + \nabla\cdot(\bar{\bar{\tau}}) + \rho\vec{g}$$

Standard $k-\varepsilon$ equations :

$$\frac{\partial}{\partial t}(\rho k) + \nabla\cdot(\rho k \boldsymbol{v}) = \nabla\cdot\left[\left(\mu + \frac{\mu_t}{\sigma_k}\right)\nabla\cdot k\right] + G_k - \rho\varepsilon + S_k$$

$$\frac{\partial}{\partial t}(\rho \varepsilon) + \nabla\cdot(\rho \varepsilon \boldsymbol{v}) = \nabla\cdot\left[\left(\mu + \frac{\mu_t}{\sigma_\varepsilon}\right)\nabla\times\varepsilon\right] + C_{1\varepsilon}\frac{\varepsilon}{k}G_k - C_{2\varepsilon}\rho\frac{\varepsilon^2}{k} + S_\varepsilon$$

$$\text{where} \mu_t = \rho C_\mu \frac{k^2}{\varepsilon}. \tag{3}$$

Scalar transport equation :

$$\frac{\partial}{\partial t}(\rho\phi_k) + \nabla\cdot(\rho\mathbf{v}\phi_k - \rho(D_m + D_t)\nabla\cdot\phi_k) = S_{\phi_k} \tag{4}$$

where

$$D_t = \frac{\mu_t}{\rho Sc_t}, \tag{5}$$

k is the kinetic energy of the turbulence, ε is its dissipation rate, G_k is the generation of turbulence kinetic energy due to mean velocity gradients, G_b is the generation of turbulence kinetic energy due to buoyancy, the other symbols are defined in the Nomenclature list and Appendix A, and "∇" refers to the del operator with respect to the spatial coordinates (X,Y). The solution of the above equations yields the flow field $\boldsymbol{v}$ and the turbulent diffusivity D_t, both of which are functions of the domain (t,X,Y). These quantities are needed in the solution of the population balance equations. The scalar transport equations for macromixing provide for species and energy transport.

2.3. Population balance equations

Spatially inhomogeneous crystallization processes can be described by the population balance equation (PBE) [47,48]

$$\frac{\partial f}{\partial t} + \sum_i^N \frac{\partial[G_i(r_i,c,T)f]}{\partial r_i} + \sum_j^3 \left\{ \frac{\partial[v_j f]}{\partial x_j} - \frac{\partial}{\partial x_j}\left[D_t \frac{\partial f}{\partial x_j}\right] \right\} = B(f,c,T)\prod_i \delta(r_i - r_{i0}) + h(f,c,T) \tag{6}$$

where the particle number density function (f) is a function of external coordinates (x_i) (X and Y in the axisymmetric case), internal coordinates (r_i) (the size dimensions of the crystal), and time (t); the rates of growth (G_i) and nucleation (B) are functions of the vector of solution concentrations (c) and the temperature (T), δ is the Dirac delta function, and h describes the creation and destruction of crystals due to aggregation, agglomeration, and breakage. For size-dependent growth, the rate of growth G_i also varies with r_i.

Unlike the PBEs most commonly used in this literature, this PBE depends on external coordinates (the mixer positions X and Y) and internal coordinates (a representative set of dimensions of the crystal that define crystal size). The use of a single dimension r for the internal coordinate implicitly assumes that the crystals have uniform shape, with any asymmetry in crystal shape addressed by a shape factor. As the solution concentrations and temperature vary with spatial position and time, Eq. (6) must be solved simultaneously with the bulk transport equations for mass, energy, momentum, and turbulence to obtain $f(\boldsymbol{x},r,t)$, $c(\boldsymbol{x},t)$, $T(\boldsymbol{x},t)$, the velocity field $\mathbf{v}(\mathbf{x},t)$, and the local turbulent diffusivity $D_t(\mathbf{x},t)$. This simulation enables the determination of the effects of the localized solution environment on the nucleation and growth rates, as well as on the CSD. The values for $\mathbf{v}$ and D_t are obtained by solving the momentum and turbulence conservation equations of the liquid phase, respectively. Equation (6) assumes that the particles follow the streamlines in the flow field [48], which is a good approximation for organic pharmaceutical crystals whose density is close to the density of the liquid phase, and for primary nucleation in a crystallizer for short times. This approximation becomes less accurate as the crystals increase in size.

Due to its hyperbolic structure, the PBE can be solved by the high-resolution finite-volume method. Gunawan et al. [49] and Ma et al. [50–52] demonstrated the capability of using such methods to numerically solve multidimensional PBEs that simulate the evolution of crystal size and shape distribution. The main advantage of using the high-resolution central scheme to discretize the growth term is that its second-order accuracy allows the use of a larger Δr, while retaining the same numerical accuracy obtained by first-order methods (e.g., upwind method). This is important because the number of transport equations that can be solved in the CFD algorithm is limited. Moreover, the method does not produce spurious oscillations in the solution, which are common in second-order methods such as Lax–Wendroff. Another advantage of using the high-resolution central scheme is that the numerical dissipation depends on Δr, but not $1/\Delta t$. This is essential due to the fact that, in most cases, very small time steps, much smaller than that limited by the Courant–Friedrichs–Lewy (CFL) condition, are required to resolve the turbulent flow and concentration field in the CFD computation. Hence, this method avoids any additional numerical dissipation associated with the time discretization. Although the approach taken here is applicable to the general PBE, Eq. (6), this paper focuses on the case of only primary nucleation and size-independent growth along one internal principal axis. Details of the high-resolution central scheme are provided in Appendix B.

Focusing first only on the first two terms of Eq. (9), semidiscrete PBEs are obtained after integrating over r over each cell and canceling terms:

$$\frac{\mathrm{d}}{\mathrm{d}t}f_j(t) = \begin{cases} -\frac{1}{\Delta r}\left\{ G_{j+1/2}\left[f_j(t) + \frac{\Delta r}{2}(f_r)_j(t)\right] - G_{j-1/2}\left[f_{j-1}(t) + \frac{\Delta r}{2}(f_r)_{j-1}(t)\right]\right\}, & G>0\ (\Delta c>0)\ \text{(crystal growth)} \\ -\frac{1}{\Delta r}\left\{ G_{j+1/2}\left[f_{j+1}(t) - \frac{\Delta r}{2}(f_r)_{j+1}(t)\right] - G_{j-1/2}\left[f_j(t) - \frac{\Delta r}{2}(f_r)_j(t)\right]\right\}, & G<0\ (\Delta c<0)\ \text{(crystal dissolution)} \end{cases} \tag{7}$$

where f_j is the cell-averaged population density in $\#/m_c\text{-}m^3$, based on Eq. (B.7) and the derivatives, $(f_r)_j$, are approximated by the minmod limiter, defined in Eqs. (B.7) and (B.8). Note that the growth rates are evaluated at the end points of each grid cell. The supersaturation $\Delta c = c - c^*$, where c^* is the solubility of the solute.

The nucleation term is included in the cell corresponding to the nuclei size by averaging the nucleation rate (the number of nuclei per unit time per unit volume) over the cell width, $B/\Delta r$. The computation of the average population density for the first grid cell, f_1, requires the values of f_0 and f_{-1}, which are fictitious points with population densities of zero at all times. The computation of f_N in the last grid cell assumes that $f_{N+1} = f_{N+2} = f_N$ at all times, which is known as the absorbing boundary condition [53].

Because the transport equations solved by the CFD algorithm are already written on a mass basis, Eq. (7) was rewritten on a mass basis to allow for easily coupling between the two sets of equations. Thus, when this equation is coupled with the transport equations of other species present in the system (solute, solvent, and antisolvent), also written on a mass basis, the overall mass balance of the system is also satisfied. The cell-averaged crystal mass in the jth size bin can be evaluated as

$$f_{w,j} = \frac{\rho_c k_v}{\Delta r}\int_{r_{j-1/2}}^{r_{j+1/2}} r^3 f_j dr = \frac{\rho_c k_v f_j}{4\Delta r}\left((r_{j+1/2})^4 - (r_{j-1/2})^4\right), \tag{8}$$

where $f_{w,j}$ has the units $kg/m_c - m^3$, and $\Delta r = r_{j+1/2} - r_{j-1/2}$. The transport equation for crystal mass between size $r_{j-1/2}$ and $r_{j+1/2}$ is

$$\frac{\mathrm{d}}{\mathrm{d}t}f_{w,j}+\sum_{i}^{3}\left\{\frac{\partial[v_i f_{w,j}]}{\partial x_i}-\frac{\partial}{\partial x_i}\left[D_t\frac{\partial f_{w,j}}{\partial x_i}\right]\right\}=\begin{cases}\dfrac{\rho_c k_v}{4\Delta r}\left[(r_{j+1/2})^4-(r_{j-1/2})^4\right]\left\{-G_{j+1/2}\left[f_j+\dfrac{\Delta r}{2}(f_r)_j\right]+G_{j-1/2}\left[f_{j-1}+\dfrac{\Delta r}{2}(f_r)_{j-1}\right]+\underset{j=0}{\mathrm{B}}\right\}, & \Delta c>0\\ \dfrac{\rho_c k_v}{4\Delta r}\left[(r_{j+1/2})^4-(r_{j-1/2})^4\right]\left\{-G_{j+1/2}\left[f_{j+1}-\dfrac{\Delta r}{2}(f_r)_{j+1}\right]+G_{j-1/2}\left[f_j-\dfrac{\Delta r}{2}(f_r)_j\right]\right\}, & \Delta c<0\end{cases} \tag{9}$$

When micromixing effects are not important, Eq. (9) can be directly incorporated into the CFD code as a transport equation by treating the right-hand side as an additional source term. A corresponding source term is added to the solute transport equation to account for its depletion due to nucleation and crystal growth, or its increment due to crystal dissolution, which is a negative sum of Eq. (9) for $j = 1, \ldots, N$.

2.4. Micro-mixing equations

Finer or subgrid scale mixing of fluids, which must precede crystallization, requires a joint composition probability distribution function [41]. This PDF will depend on position and time, and its evolution can be followed by solution of the transport equation. Because of the many system variables in the PDF, the transport equation cannot be solved by standard discretization methods and is best solved by Monte Carlo methods [54].

A good alternative to the Monte Carlo solution of the transported PDF is the multienvironment CFD micromixing model proposed by Fox [41] and applied to crystallization by Fox and associates [54–58]. This model, also known as the finite-mode PDF method, is used to model micromixing effects [38–40]. In this approach, each computational cell in the CFD grid is divided into N_e different probability modes or environments, which correspond to a discretization of the presumed composition PDF into a finite set of delta (δ) functions:

$$f_\phi(\boldsymbol{\psi};\mathbf{x},t)=\sum_{n=1}^{N_e}p_n(\mathbf{x},t)\prod_{\alpha=1}^{N_s}\delta\left[\psi_\alpha-\langle\phi_\alpha\rangle_n(\mathbf{x},t)\right] \tag{10}$$

where f_φ is the joint PDF of all scalars, N_s is the total number of scalars (species), p_n is the probability of mode n or volume fraction of environment n, and $\langle\phi_\alpha\rangle_n$ is the mean composition of scalar α corresponding to mode n, and ψ_α is the element of $\boldsymbol{\psi}$ corresponding to the scalar α. The weighted concentration is defined as

$$\langle\mathbf{s}\rangle_n\equiv p_n\langle\phi\rangle_n \tag{11}$$

The transport of probability and species in inhomogeneous flows is modeled by

$$\frac{\partial\mathbf{p}}{\partial t}+\sum_i\left[\langle v_i\rangle\frac{\partial\mathbf{p}}{\partial x_i}-\frac{\partial}{\partial x_i}(D_t\frac{\partial\mathbf{p}}{\partial x_i})\right]=\mathbf{G}(\mathbf{p})+\mathbf{G_s}(\mathbf{p}) \tag{12}$$

$$\frac{\partial\langle\mathbf{s}\rangle_n}{\partial t}+\sum_i\left[\langle v_i\rangle\frac{\partial\langle\mathbf{s}\rangle_n}{\partial x_i}-\frac{\partial}{\partial x_i}(D_t\frac{\partial\langle\mathbf{s}\rangle_n}{\partial x_i})\right]=\mathbf{M}^n(\mathbf{p},\langle\mathbf{s}\rangle_1,\ldots,\langle\mathbf{s}\rangle_{N_e})+\mathbf{M}^n_\mathbf{s}(\mathbf{p},\langle\mathbf{s}\rangle_1,\ldots,\langle\mathbf{s}\rangle_{N_e})+p_n\mathbf{S}(\langle\phi\rangle_n) \tag{13}$$

where $\boldsymbol{G}$ and $\boldsymbol{M^n}$ are the rates of change of $\mathbf{p} = [p1\ p2\ \ldots\ pN]$ and $\langle\mathbf{s}\rangle_n$ due to micromixing, respectively, $\boldsymbol{G}_\mathrm{s}$ and $\mathbf{M}^n_\mathbf{s}$ are additional micromixing terms to eliminate the spurious dissipation rate in the mixture–fraction–variance transport equation (for details see Fox [41]), and $\mathbf{S}$ is the chemical source term. The conservation of probability requires that

$$\sum_{n=1}^{N}p_n=1 \tag{14}$$

and

$$\sum_{n=1}^{N_e}G_n(\mathbf{p})=0. \tag{15}$$

The mean compositions of the scalars are given by

$$\langle\phi\rangle=\sum_{n=1}^{N_e}p_n\langle\phi\rangle_n=\sum_{n=1}^{N_e}\langle\mathbf{s}\rangle_n \tag{16}$$

and, since the means remain unchanged by micromixing,

$$\sum_{n=1}^{N_e}\mathbf{M}^n(\mathbf{p},\langle\mathbf{s}\rangle_1,\ldots,\langle\mathbf{s}\rangle_{N_e})=0 \tag{17}$$

must be satisfied. The simulations in this article utilize a three-environment model, as shown in Fig. 2. This approach was used by Marchisio et al. [55–57] to model precipitation using the method of moments to model the average properties of the crystalline phase. They suggested that three environments are sufficient to capture the micromixing effects in non-premixed flows with satisfactory accuracy. The extension to a larger number of environments is possible [41,54,58], but at a larger computational burden, as one set of semidiscrete PBE has to be solved in each mixed environment. An advantage of this multienvironment PDF model is that it can be directly incorporated into existing CFD codes, in which the transport Eqs. (12) and (13) can be computed directly by the CFD solver. Since the compositions in Environments 1 and 2 are known from the composition of the feed and initial conditions, Eq. (13) will be applied to all species in Environment 3 only. This third environment includes solute, solvent, antisolvent, and the crystal mass in each grid cell of the semidiscrete PBE. Another important variable evaluated by Eq. (13) is $\langle\xi\rangle_3$, the mixture fraction in Environment 3, which represents the fraction of fluid in Environments 3 that came from Environment 1. The mixture fractions in Environments 1 and 2 are $\langle\xi\rangle_1 = 1$ and $\langle\xi\rangle_2 = 0$, respectively. With $N_e = 3$, it is possible to calculate the mean, variance, and skewness of the mixture fraction. However, this paper will utilize the population balance equations,

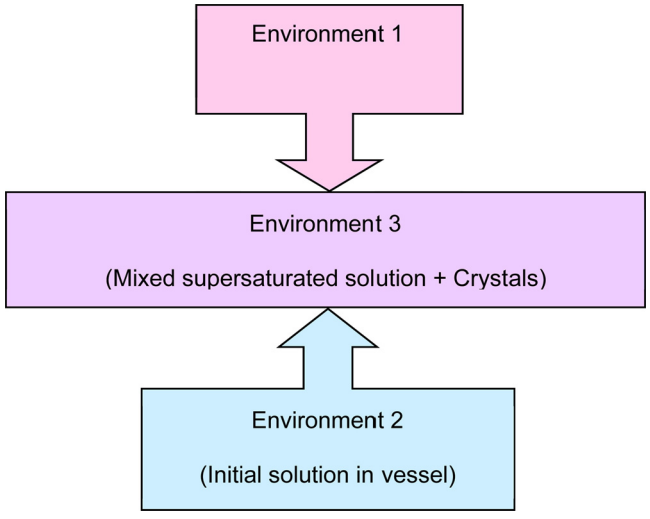

Fig. 2. Three-environment micromixing model.

Table 1
Micromixing terms.

Model variables	$G,\mathbf{M}^n$	$G,\mathbf{M}_s^n$
p_1	$-\gamma p_1(1-p_1)$	$\gamma_s p_3$
p_2	$-\gamma p_2(1-p_2)$	$\gamma_s p_3$
p_3	$\gamma[p_1(1-p_1)+p_2(1-p_2)]$	$-2\gamma_s p_3$
$\langle\mathbf{s}\rangle_3$	$\gamma[p_1(1-p_1)\langle\boldsymbol{\Phi}\rangle_1+p_2(1-p_2)\langle\boldsymbol{\Phi}\rangle_2]$	$-\gamma_s p_3(\langle\boldsymbol{\Phi}\rangle_1+\langle\boldsymbol{\Phi}\rangle_2)$
	$\gamma=\dfrac{\varepsilon_\xi}{p_1(1-p_1)(1-\langle\xi\rangle_3)^2+p_2(1-p_2)\langle\xi\rangle_3^2}$	
	$\gamma_s=\dfrac{2D_t}{(1-\langle\xi\rangle_3)^2+\langle\xi\rangle_3^2}\dfrac{\partial\langle\xi\rangle_3}{\partial x_i}\dfrac{\partial\langle\xi\rangle_3}{\partial x_i}$	
	$\langle\xi'^2\rangle=p_1(1-p_1)-2p_1p_3\langle\xi\rangle_3+p_3(1-p_3)\langle\xi\rangle_3^2$	

discussed in Section 2, to compute the full crystal size distribution (CSD).

The micromixing terms [41] are summarized below in Table 1, where the values of $\langle\boldsymbol{\Phi}\rangle_n = \langle\mathbf{s}\rangle_n/p_n$ denote the unweighted variables. The value of p_3 can also be determined from Eq. (14), although numerical error may lead to an inaccurate result when P_1+P_2 is close to 1. For a fully-developed scalar spectrum, the scalar dissipation rate, ε_ξ, is related to the turbulent frequency, ε/k, by

$$\varepsilon_\xi = C_\varphi\langle\xi'^2\rangle\frac{\varepsilon}{k} \tag{18}$$

where $C_\varphi = 2$ (as suggested by Wang and Fox [54]), ε and k are the turbulent dissipation rate and kinetic energy, respectively, and $\langle\xi'^2\rangle$ is the mean variance of the mixture fraction $\langle\xi\rangle_3$. The chemical source terms in Eq. (13) for the solute and crystals are substituted with the right-hand side of Eq. (9) along with the appropriate nucleation and growth kinetics that are not limited by micromixing. For unseeded crystallization, the micromixing terms for the crystals are zero.

Due to the adiabatic operation of the coaxial mixer/crystallizer, a simple calculation can be made to estimate the effect of the heats of crystallization and mixing on temperature. Heat of mixing results from mixing the solute-containing fluid with the anti-solvent fluid. This micromixing initially releases heat in Environment 3. Likewise, the crystallization of the solute occurs mostly in Environment 3, so the heat of crystallization is released there as well. If the interphase (or inter-environmental) transport of this released heat is ignored, all of it stays in Environment 3. The heat eventually gets distributed to all of the fluid in the mixer as Environment 3 grows at the expense of Environments 1 and 2. Under these assumptions, the temperature increase is calculated by tracking the enthalpy (kJ/m^3) in Environment 3 as a scalar using Eq. (13). If the inner and outer input streams are at different temperatures, then the enthalpies of Environments 1 and 2 need to be specified. The value of the enthalpy in Environment 3 results from the micro-mixing of Environments 1 and 2 (the M terms in Eq. (13)), the heat of mixing due to change in the intermolecular neighborhood of each antisolvent molecule, and the heat of crystallization of the solute. The latter two are incorporated into the source term p_3S, which for the weighted enthalpy h is expressed as

$$p_3S_h = p_3\frac{(S_{as_1})(-\Delta H_{\mathrm{mix,H_2O-CH_3OH}})}{\mathrm{MW}_{\mathrm{H_2O}}} + p_3\frac{\left(\sum_j S_{f_{w,j}}\right)(-\Delta H_{\mathrm{crys}})}{\mathrm{MW}_{\mathrm{solute}}} \tag{19}$$

where S_{as} and $\left(\sum_j S_{f_{w,j}}\right)$ are the rates of increase in concentrations of antisolvent and total crystal mass in Environment 3, and the other symbols are defined in Appendix A. This calculation is handled in the UDF file (see below), along with other micromixing phenomena. The subscript as_1 denotes the concentration of water in the antisolvent, $-\Delta H_{\mathrm{mix,H_2O-CH_3OH}}$ is the heat of mixing of methanol with water, $-\Delta H_{\mathrm{crys}}$ is the heat of crystallization of lovastatin from a methanol–water mixture, and the other symbols are defined in Appendix A. The values of $\Delta H_{\mathrm{mix,H_2O-CH_3OH}}$ depend on the mole fraction of methanol in the mixture and are taken from Bertran et al. [59] The heat of crystallization $-\Delta H_{\mathrm{crys}}$ is derived from a van't Hoff relation used to fit the solubility data (see next section). Following Fox [41], the rate of change S_T of temperature in Environment 3 is obtained from

$$S_T = \frac{S_h}{\rho_3 C_{p3}} \tag{21}$$

2.5. Crystallization kinetics of lovastatin

A solubility relation is essential to compute the relative supersaturation, which represents the driving force for the rates of nucleation and growth. Solubility data for lovastatin in a methanol/water mixture were used by Woo et al. [40] to compute supersaturation in a confined impinging jet mixer. Solubilities at other temperatures were obtained from Tung et al. [60] and Sun et al. [61] The combined data from all three sources were fitted to the expression

$$c^*\left(\frac{\mathrm{kg}}{\mathrm{kg}}\text{of solvents}\right) = 0.001\exp(15.45763\left(1-\frac{1}{\theta}\right)\left\{\begin{array}{ll} -2.7455\times10^{-4}W_{as}^3+3.3716\times10^{-2}W_{as}^2-1.6704W_{as}+33.089, & \text{for} W_{as}\le 45.67 \\ -1.7884\times10^{-2}W_{as}+1.7888, & \text{for} W_{as}>45.67 \end{array}\right\} \tag{22}$$

where W_{as} is the weight percent of antisolvent (H_2O) on a solute-free basis and the dimensionless temperature θ is

$$\theta = \frac{T}{T_{\mathrm{ref},}} \tag{23}$$

where T is the absolute temperature, T_{ref} is the reference temperature of 296 K, and the coefficient 15.45763 in the temperature-dependence factor implies a heat of crystallization value of $-\Delta H_{\mathrm{crys}} = 38{,}042.5$ kJ/kmol.

Based on the crystallization kinetics [43] of lovastatin from a methanol–water mixture, the dependencies of primary nucleation and growth kinetics upon relative supersaturation S are:

$$B = B_{\text{homogeneous}} + B_{\text{heterogeneous}}$$

$$B_{\text{homogeneous}} \quad \text{at } 23^{\circ}\text{C}(/\text{m}^3\text{s}) = 6.97 \times 10^{14}\exp\left(\frac{-15.8}{[\ln S]^2}\right) \tag{24}$$

$$B_{\text{heterogeneous}} \quad \text{at } 23^{\circ}\text{C}(/\text{m}^3\text{s}) = 2.18 \times 10^{8}\exp\left(\frac{-0.994}{[\ln S]^2}\right)$$

$$G \quad \text{at } 23^{\circ}\text{C}(\text{m/s}) = 8.33 \times 10^{-30}(2.46 \times 10^{3}\ln S)^{6.7} \tag{25}$$

According to Mahajan and Kirwan [43], crystal growth for the lovastatin/methanol–water system is surface-integration limited, and the growth rate is size-independent. Woo et al. [40] suggest that secondary nucleation can be neglected due to the small solids density in impinging jets, and this same assumption is made for the coaxial mixer/crystallizer.

The simulation was carried out with methanol saturated with lovastatin at 305 K in the outer inlet and liquid H_2O at 293 K in the inner inlet. The outer stream is designated as Environment 1 in the micromixing model, while the inner stream is designated as Environment 2. In the UDF file linked to Fluent (see Section 3), methanol (MOH) is designated as the solvent, and the antisolvent is pure liquid water. The material properties for the two input streams and the mixed fluid, designated as Environment 3, are computed by Fluent using appropriate mixture rules.

The density of lovastatin is 1273 kg/m^3, and the volume shape factor was assumed to be 0.000625. The population balance equation was discretized into 30 bins for the longest growth axis, with $\delta r = 8\ \mu$m. The use of effective viscosity, as described in Woo et al. [38], was omitted because the solid fraction was too small to significantly affect the effective viscosity.

3. Fluent program and scope of calculations

3.1. Fluent

Calculations were performed by the computational fluid dynamic (CFD) code Fluent [45], which is owned by Ansys [46]. The axisymmetric geometric design and spatial mesh of the coaxial nozzle was built by Gambit of the pre-Ansys Fluent program, although the DesignModeler feature of Ansys can also be used, which provided the X–Y grid of cells, with X representing the axial position and Y representing the radial or transverse position. The proper turbulence model (standard k-epsilon with enhanced wall treatment), the energy equation, and the species transport equation were selected. The physical properties of the entering fluids, methanol and water, were provided by built-in features of Fluent, and the code also computes properties of the mixed fluid.

User-defined Function (UDF) files are used to link complex subsystems of equations into the overall FLUENT code. In the mixer/crystallizer application, the PBE, crystallization kinetics, and micromixing equations are linked to the CFD portion of the code by a UDF. This portion of the code allows important changes to be made without going through the lengthy setup steps in Fluent. Up to three solvents and antisolvents can be handled, but the calculations reported here involve only a single solvent and antisolvent.

3.2. Scalars tracked by calculations

Table 2 lists the variables tracked in the CFD code using User Defined Scalar (UDS) transport equations. The first three variables are the volume fractions of the three environments, while the fourth and fifth variables are the mixture fraction in Environment 3 and the weighted mixture fraction in Environment 3, respectively. Since the UDSs have the ability to handle up to three solvents and three antisolvents, the next seven UDSs are weighted compositions of the mixture components (solutes, antisolvents, and solvents). Since this particular study involves only one solute, one antisolvent, and one solvent, only three of these UDSs will ever be nonzero. The final thirty are the mass density functions in the 30 size bins.

Table 2
Scalars calculated using user defined file in fluent.

j	Variable	Equation used
1	p_1	(12)
2	p	(12)
3	p_3	(12)
4	$\langle\xi\rangle_3$	(13)
5	$p_3\langle\xi\rangle_3$	(13)
6–12	$p_3\langle s_i\rangle_3$	(13)
13–42	$f_{w,j}$	(9)

3.3. Types of calculations

Simulations were performed using a 0.01816 m radius and 1.0 m long coaxial nozzle. In the inlet zone, which is 0.1 m long, the solvent/solute mixture was fed into the outer annulus (the method and the code described in the manuscript are both general enough to handle the case in which the position of the solvent/solute mixture and antisolvent streams are switched). The inner radius of this annulus was 0.007264 m, and the outer radius was 0.01816 m. The antisolvent was fed into the inner tube, which had an inner radius of 0.003911 m. The separation wall in the inlet zone was tapered over the last 0.05 m to provide a small component of radial velocity to the antisolvent stream. A diagram of the front portion of the coaxial nozzle is shown in Fig. 3.

For the antisolvent stream, pure water was used, and the inlet temperature was set 293 K. The temperature of the solvent/solute (methanol/lovastatin) mixture was set at 305 K, which gives a saturated concentration of lovastatin in pure methanol that is 0.0237 kg solute/kg solute free solvent higher than that at 293 K. Heat transfer through the inner and outer tubes is neglected in the simulations.

For the transient model, which can be run to achieve steady state, the values of the flow variables and user-defined scalar variables were set initially to describe antisolvent (pure water) flowing through both regions of the nozzle. At time zero, the solvent/solute stream was then started through the annular input region.

Calculations reported in this paper represent two sets of conditions. The first set of calculations begins with a solvent (methanol) flow rate MF_o of 0.707 kg/s and an antisolvent (water) flow rate MF_i of 0.368 kg/s. Subsequent calculations are made for 0.707 kg/s of methanol and increasing mass inputs of water: $MF_o = 0.707$ kg/s, $MF_i = 0.53$ kg/s; $MF_o = 0.707$ kg/s, $MF_i = 0.70$ kg/s; $MF_o = 0.707$ kg/s, $MF_i = 0.80$ kg/s; and $MF_o = 0.707$ kg/s, $MF_i = 0.90$

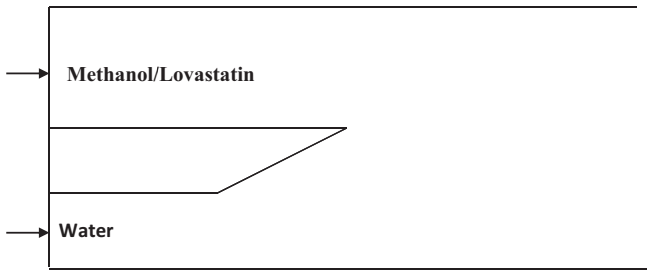

Fig. 3. Entrance zone of coaxial nozzle.

Table 3
Conditions for variable antisolvent to solvent ratio.

Methanol mass flow (kg/s)	Water mass flow (kg/s)	Residence time in mixing zone (s)	Maximum turbulence Reynolds number	% Solute crystallized at $X = 1.0$ m
0.707	0.368	0.733	8206	58.11
0.707	0.510	0.659	12000	78.83
0.707	0.610	0.616	15287	78.23
0.707	0.700	0.581	18414	77.78
0.707	0.800	0.547	21855	77.31
0.707	0.900	0.516	25250	76.90

kg/s. The second set of calculations involves holding the ratio of antisolvent to solvent flow rates at 0.70–0.707. The total mass input was changed to examine the effect of turbulence on crystallization. The three pairs of input flow rates are: 0.536 kg/s methanol, 0.53 kg/s water; 0.707 kg/s methanol, 0.70 kg/s water; and 0.910 kg/s methanol, 0.90 kg/s water.

4. Results for variable antisolvent/solvent flow ratios

The ratio of inner (antisolvent fluid) flow to annular (solvent/solute fluid) flow was increased to examine its effect crystallization. Table 3 shows the nozzle flow conditions and percentage of input solute that was crystallized.

The associated crystal size distributions corresponding to various axial locations are plotted in Figs. 4–6. For lower water to methanol flow ratios (0.368–0.700 kg/s CH_3OH to 0.707 kg/s H_2O), the crystal size distribution (CSD) is biased toward the smaller sizes. At higher flow ratios, 0.80–0.90 kg/s H_2O to 0.707 kg/s of methanol, the CSD is less dominated by smaller crystals, and the larger-size ranges increase in population density. This could be due to the increased turbulence from a higher total flow rate, which provides rigorous mixing and higher concentration of antisolvent fluid in the crystallization zone. The higher concentration of antisolvent plays a role in accelerating crystallization by decreasing the saturated concentration of lovastatin (see Eq. (22)), thus contributing more to supersaturation. For an antisolvent flow rate of 0.900 kg/s, there is a slight dilution of the solute concentration by the additional antisolvent, but the net effect is an increase in relative supersaturation and enhanced nucleation and crystallization. The increased flow rate also corresponds to a moderately shorter residence time, yielding slightly less crystallization, as shown in Table 3.

As the antisolvent to solvent/solute ratio changed in addition to the total fluid flow rate, it is difficult to determine the effect of the latter on mixing and crystallization. This uncertainty led to the computations discussed in Section 5.

5. Results for variable total mass flow rates

5.1. Comparisons

Table 4 gives various total mass flow rates for the solvent and antisolvent flow rates with the antisolvent/solvent ratio held constant at 0.99, which ensures adequate antisolvent according to Table 3. The purpose was to show the effect that turbulence had on mixing and crystallization. Contour plots are given for several

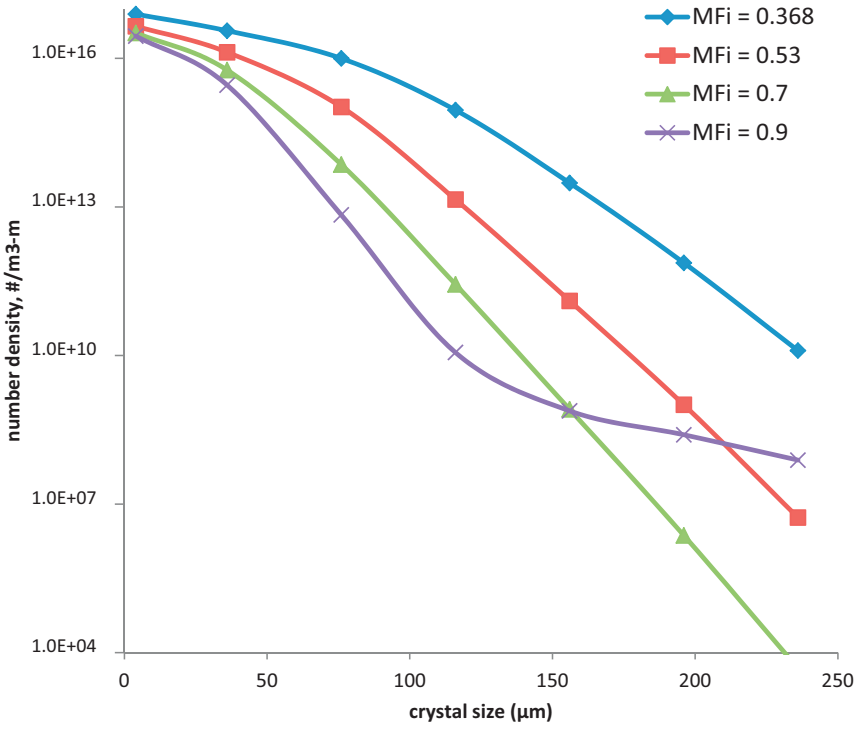

Fig. 4. Crystal size distribution at axial position $X = 0.12$ m for methanol (solvent) flow rate $MF_o = 0.707$ kg/s and various values of water (antisolvent) flow rate MF_i. The plot is on a semi-logarithmic scale, and the number density function in the last bin is more than 6 orders of magnitude smaller than the value of the function in the first bin so the fraction of crystals that could grow out of the range of 0–240 μm is negligible.

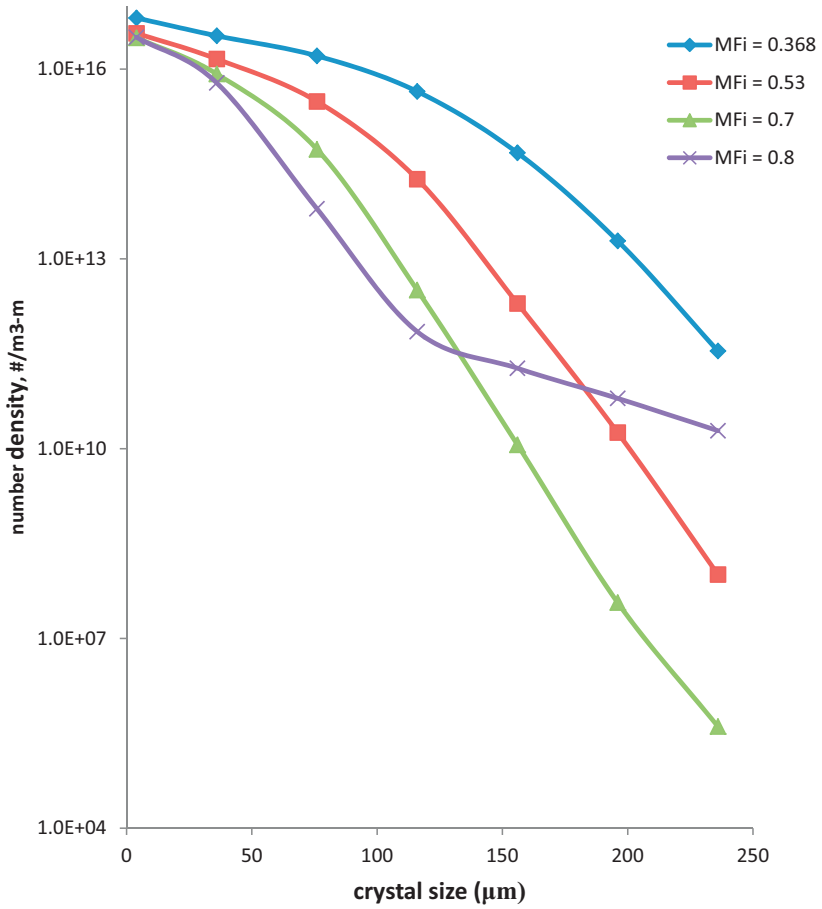

Fig. 5. Crystal size distribution at axial position $X = 0.135$ m for methanol (solvent) flow rate $MF_o = 0.707$ kg/s and various values of water (antisolvent) flow rate MF_i. The plot is on a semi-logarithmic scale, and the number density function in the last bin is more than 5 orders of magnitude smaller than the value of the function in the first bin so the fraction of crystals that could grow out of the range of 0–240 μm is negligible.

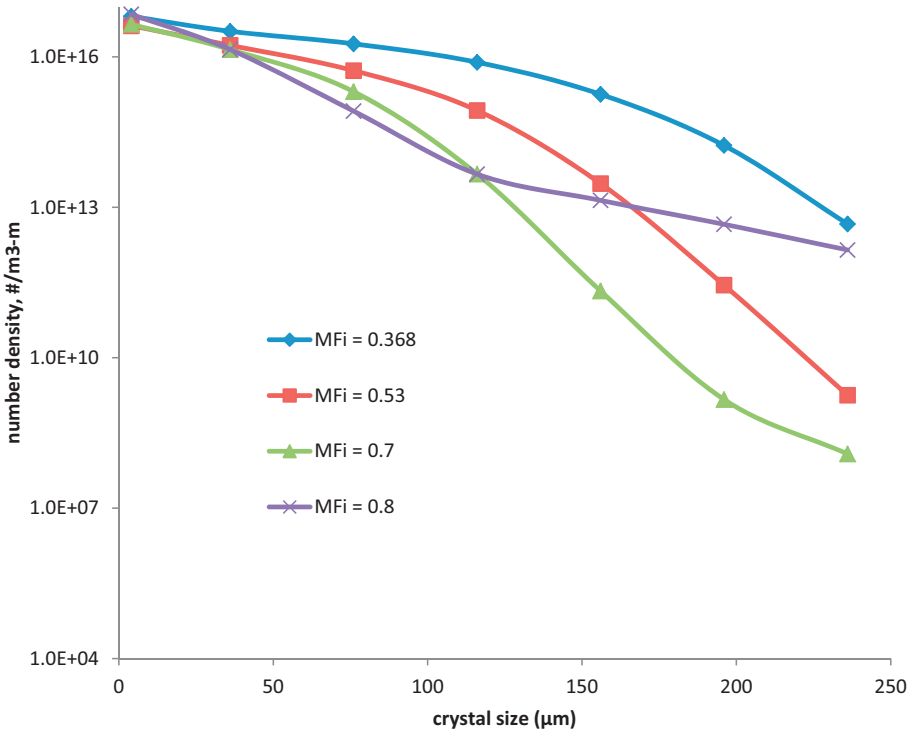

Fig. 6. Crystal size distribution at axial position $X = 0.150$ m for methanol (solvent) flow rate $MF_o = 0.707$ kg/s and various values of water (antisolvent) flow rate MF_i.

Table 4
Conditions for variable total mass flow rate.

Methanol mass flow (kg/s)	Water mass flow (kg/s)	Residence time in mixing zone (s)	Maximum turbulence Reynolds number	% Solute crystallized at $X = 0.1$ m
0.536	0.53	0.767	14152	79.47
0.707	0.70	0.581	18414	77.78
0.909	0.90	0.452	23947	76.93

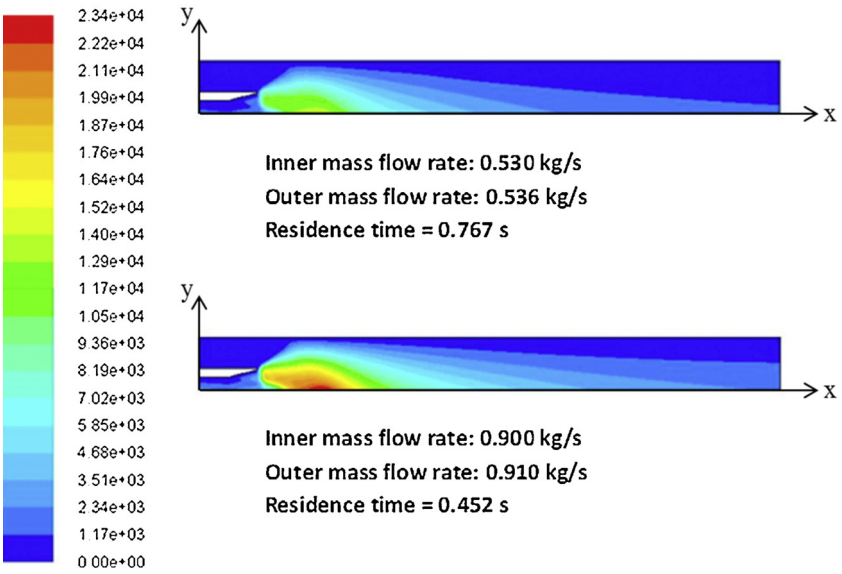

Fig. 7. Local turbulent Reynolds number in coaxial nozzle at steady state for different total mass input rates (outer inlet: methanol saturated with lovastatin, inner inlet: water, water to methanol ratio = 0.99). Upper boundary (outer wall). Lower boundary (nozzle axis). Nozzle radius = 0.01816 m, Nozzle length = 1.0 m.

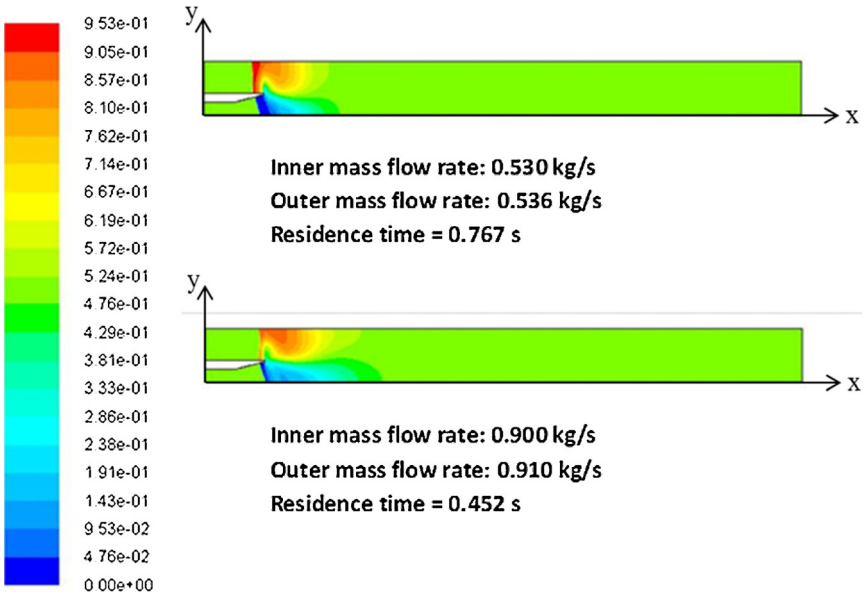

Fig. 8. Mean mixture fraction $\langle \xi \rangle_3$ in coaxial nozzle at steady state for different total mass input rates (outer inlet: methanol saturated with lovastatin, inner inlet: water, water to methanol ratio = 0.99). Upper boundary (outer wall). Lower boundary (nozzle axis). Nozzle radius = 0.01816 m, Nozzle length = 1.0 m.

important variables in Figs. 7–17. For purposes of illustration, the Y (or transverse) dimension has been expanded by a factor of 5 in order to make the contours more visible to the reader. Also, as the system is axisymmetric, only half of the mixer is shown. The center line of the mixer ($Y = 0$) is the lower boundary, and the mixer wall ($Y = 0.01816$ m) is the upper boundary. The axial length of the mixer is 1.0 m, but the entrance zone for the unmixed streams is 0.1 m, leaving 0.9 m for actual mixing. To compare the effect of input mass flow rate, results for two inlet conditions are shown. These conditions are: inner mass flow rate = 0.53 kg/s, annular mass flow

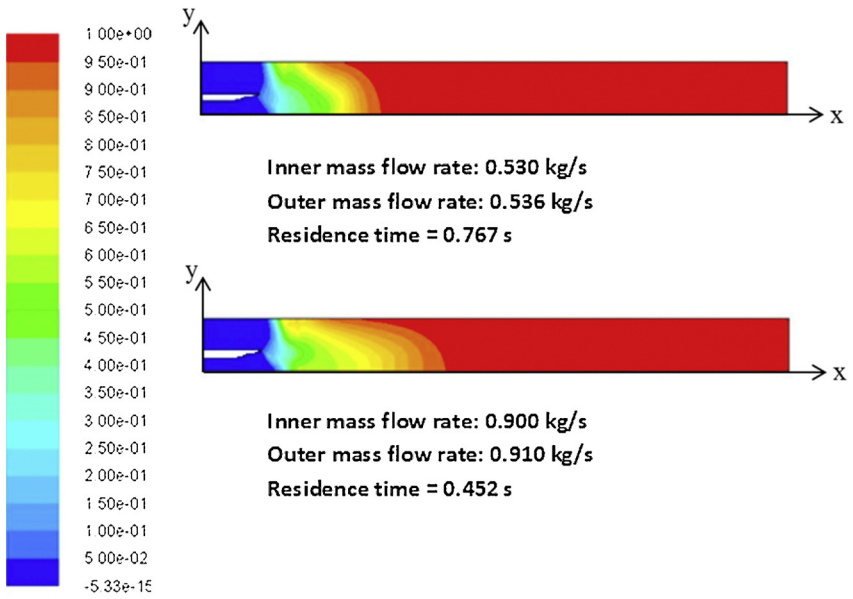

Fig. 9. Volume fraction p_3 of the mixed environment in coaxial nozzle at steady state for different total mass input rates (outer inlet: methanol saturated with lovastatin, inner inlet: water, water to methanol ratio = 0.99). Upper boundary (outer wall). Lower boundary (nozzle axis). Nozzle radius = 0.01816 m, Nozzle length = 1.0 m.

rate = 0.536 kg/s; and inner mass flow rate = 0.90 kg/s, annular mass flow rate = 0.909 kg/s. These two sets of flow rates, with a constant ratio of antisolvent to solvent flow of 0.99, correspond to total residence times in the mixing zone of the coaxial nozzle of 0.767 and 0.452 s, respectively. Thus, any axial position in a contour plot for the higher flow rate will correspond to a shorter residence time than the same axial position for the lower flow rate. In order to compare the coaxial nozzle results to the impinging jet calculations of Woo et al. [40], which involved short residence times, key variables were sampled at locations just downstream of the mixing junction in the nozzle. The shorter residence times corresponding to these locations are in the range of those used for the impinging jet mixer.

5.2. Mixing

The local turbulent Reynolds number in the coaxial nozzle is shown in Fig. 7, which has the same qualitative trend as impinging jet calculations [40,65,66]. As expected, the magnitude of turbulence increases with input mass flow, maximizing at about $X = 0.21$ m and $Y = 0.0$ m in both cases. As the length of the inner tube is 0.101 m, $X = 0.21$ m corresponds to a mixing length of 0.109 m and residence times of 0.092 and 0.054 s, respectively, for the lower and higher mass flow rates. As expected, turbulence is minimal at the tube wall, due to the no-slip condition.

As in the case of impinging jets, micro-mixing of the two input fluids is rapid. As the mixed fluid, Environment 3, begins to form at the junction of the inner and outer fluids, the fraction $\langle \xi \rangle_3$ of the

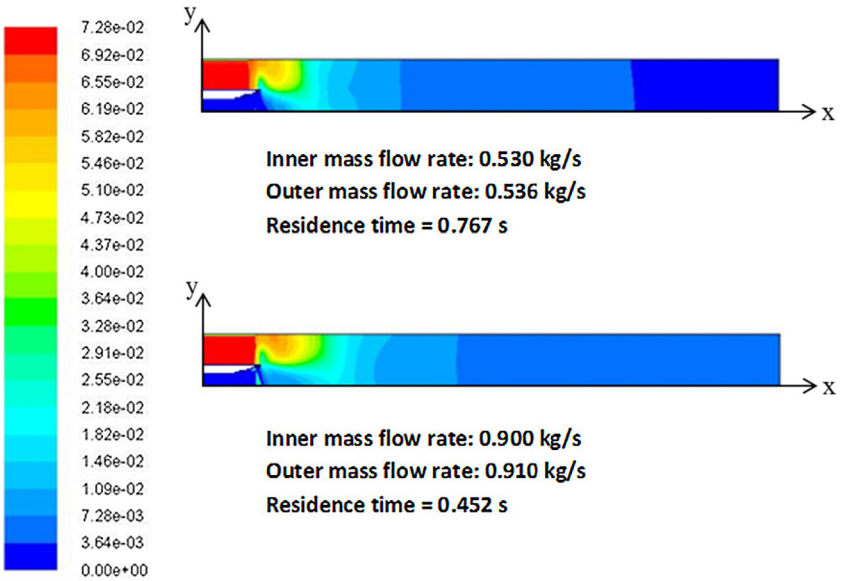

Fig. 10. Solute concentration c, (kg/kg solvents), in coaxial nozzle at steady state for different total mass input rates (outer inlet: methanol saturated with lovastatin, inner inlet: water, water to methanol ratio = 0.99). Upper boundary (outer wall). Lower boundary (nozzle axis). Nozzle radius = 0.01816 m, Nozzle length = 1.0 m.

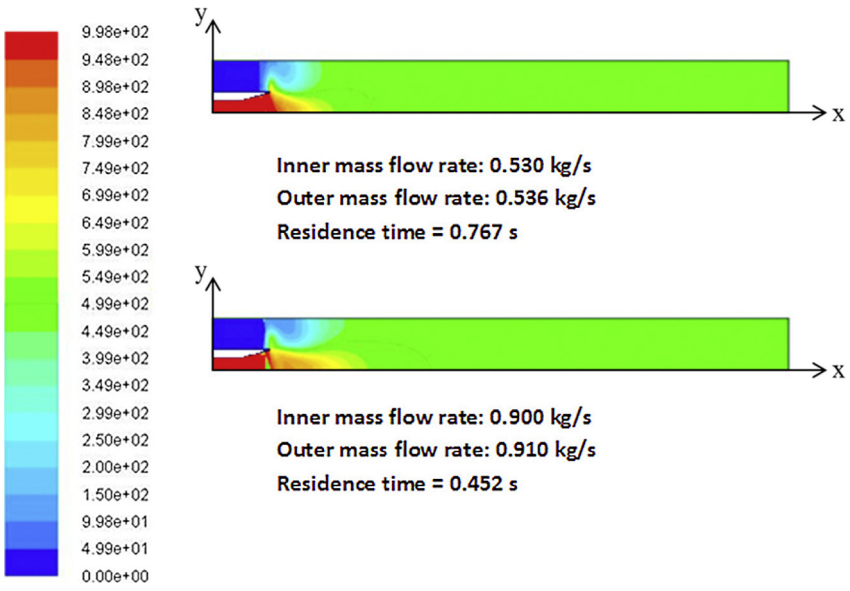

Fig. 11. Antisolvent concentration a_s (kg/m$_3^3$) within environment 3 in coaxial nozzle at steady state for different total mass input rates (outer inlet: methanol saturated with lovastatin, inner inlet: water, water to methanol ratio = 0.99). Upper boundary (outer wall). Lower boundary (nozzle axis). Nozzle radius = 0.01816 m, Nozzle length = 1.0 m.

mixed fluid that is formed from Environment 1 is higher in the outer region of the nozzle, as expected (see Fig. 8). For the higher input flow conditions, the mixing is faster and more extensive, requiring a mixing time of only 0.085 s to achieve the completely mixed value (called the stoichiometric value) of $\langle\xi\rangle_3 = 0.51$, as compared to the 0.112 s required in the low flow case. In either case, less than 0.194 m (or a fifth) of the mixing zone is required for complete mixing.

As shown in Fig. 9, the volume fraction p_3 of the mixed environment, mass-averaged over the cross-section, reaches 0.95 at $X = 0.31$ m for the low input flow case, which corresponds to a residence time of 0.173 s. For the high input flow rate, the residence time required to achieve a mass-based cross-sectional average of 0.95 for p_3 (at $X = 0.41$ m) is only 0.155 s, thus showing that increased turbulence enhances micro-mixing.

5.3. Crystallization dynamics

As shown in Fig. 10, the solute concentration c declines more quickly down the crystallizer for the lesser flow case than the higher flow case, which is expected because the residence time is higher for the former condition. The antisolvent concentration is presented in Fig. 11, while contours for the saturated solute concentration c^* are illustrated in Fig. 12. Just downstream of the junction of the two inlets, the antisolvent (Environment 2) is sufficiently mixed with the solution (Environment 1), so c^* drops by an order of magnitude, in agreement with Eq. (22). The relative supersaturation S, shown in Fig. 13, has a contour pattern that is obviously correlated with antisolvent concentration, as does the nucleation rate B (Fig. 14), and the crystal growth rate G (Fig. 15). The latter two correlations are expected due to Eqs. (24) and (25).

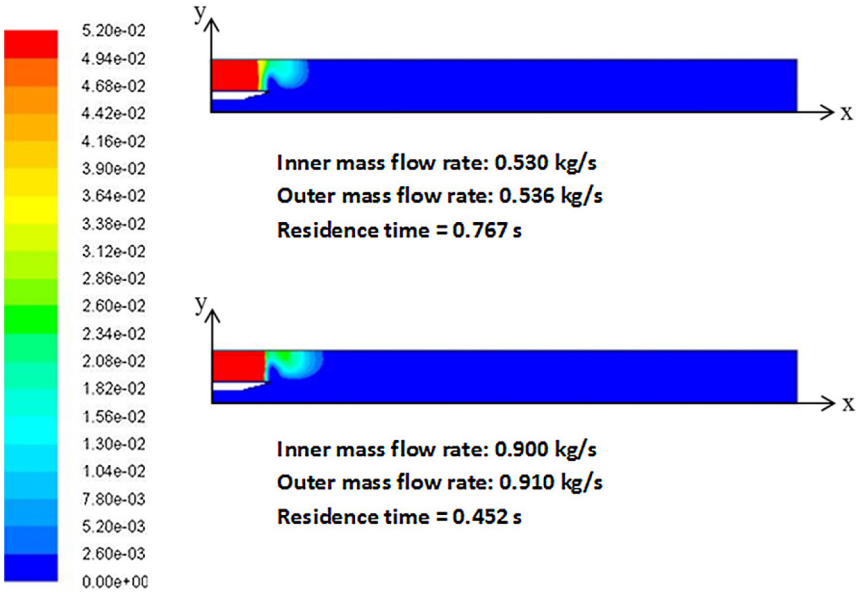

Fig. 12. Saturated solute concentration c^* (kg/kg solvents) in coaxial nozzle at steady state for different total mass input rates (outer inlet: methanol saturated with lovastatin, inner inlet: water, water to methanol ratio = 0.99). Upper boundary (outer wall). Lower boundary (nozzle axis). Nozzle radius = 0.01816 m, Nozzle length = 1.0 m.

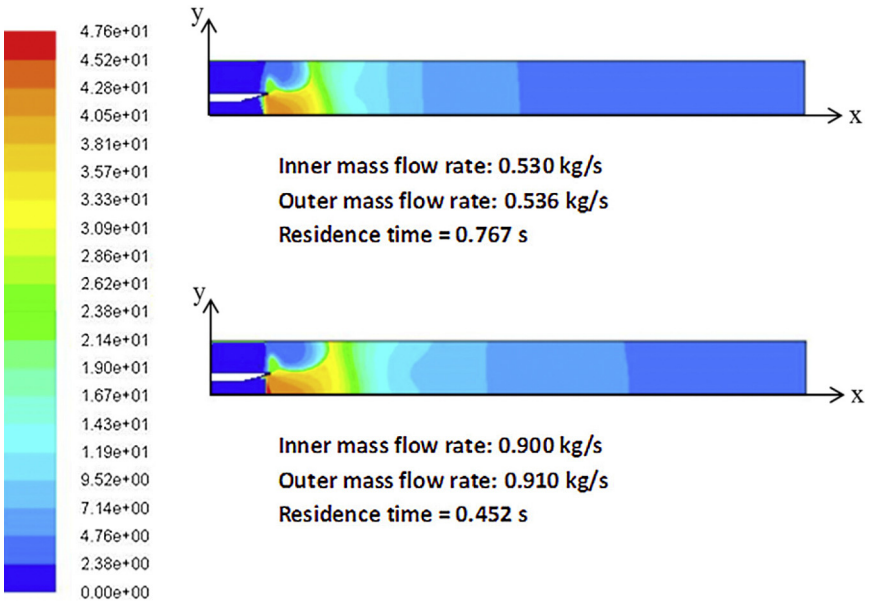

Fig. 13. Supersaturation S ($= c/c^*$) in the coaxial nozzle at steady state for different total mass input rates (outer inlet: methanol saturated with lovastatin, inner inlet: water, water to methanol ratio = 0.99). Upper boundary (outer wall). Lower boundary (nozzle axis). Nozzle radius = 0.01816 m, Nozzle length = 1.0 m.

All these variables reach their maxima on the nozzle axis (center), and slightly downstream of the mixing junction. At the higher input mass flow rate, the equivalent residence times are greater at any given axial location X; thus, the maximal regions of B and G are more spread out spatially.

The total mass density of crystals $\sum_{j=1}^{j=N_{cell}} f_{w,j}$ is shown in Fig. 16. Not surprisingly, the distance required to achieve a total mass density of 24 kg/m^3 is larger for the higher input rate. As indicated in Table 4, only 76.9–79.5% of crystallization is accomplished within $X = 1.0$ m. In order to achieve more complete crystallization, it is obvious that the nozzle length will need to be increased to provide more residence time, or the nozzle output should be discharged into a holding tank.

5.4. Temperature and heats of mixing and crystallization

Temperature contours for the two total flow rates are compared in Fig. 17. Other than turbulent diffusion, three major phenomena are responsible for the spatial variation in temperature: (1) mixing of warmer and colder fluids entering the mixing tube; (2) heat of mixing due to disruption of H_2O–H_2O intermolecular forces by intruding CH_3OH molecules; and (3) heat released by crystallization of lovastatin from the methanol–water mixture.

Recall that the entrance temperature of the solute-containing fluid is 305 K, while that of the antisolvent-containing fluid is 293 K. As the two input fluids mix, the solute is exposed not only to antisolvent but to a lower temperature as well. Both effects lower solubility of the solute. Heats of mixing and crystallization negate

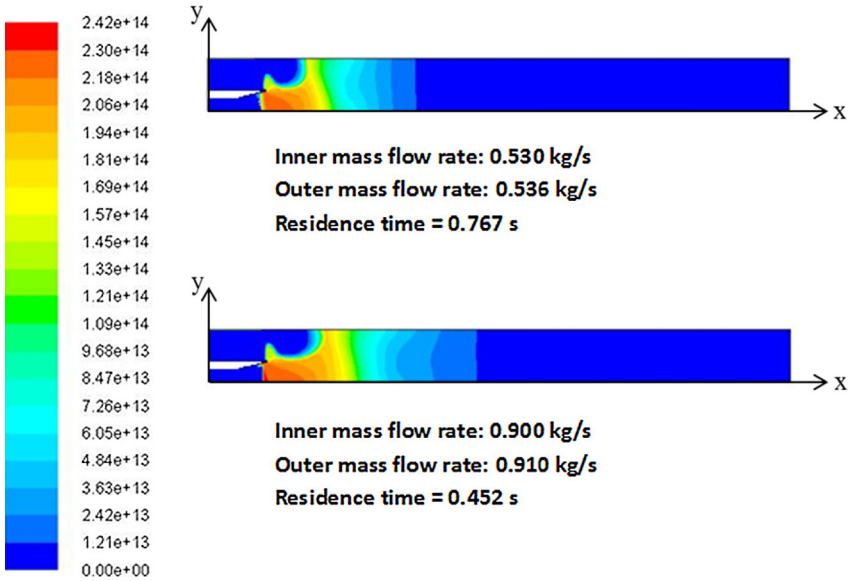

Fig. 14. Nucleation rate B (#/s m^3) in the coaxial nozzle at steady state for different total mass input rates (outer inlet: methanol saturated with lovastatin, inner inlet: water, water to methanol ratio = 0.99). Upper boundary (outer wall). Lower boundary (nozzle axis). Nozzle radius = 0.01816 m, Nozzle length = 1.0 m.

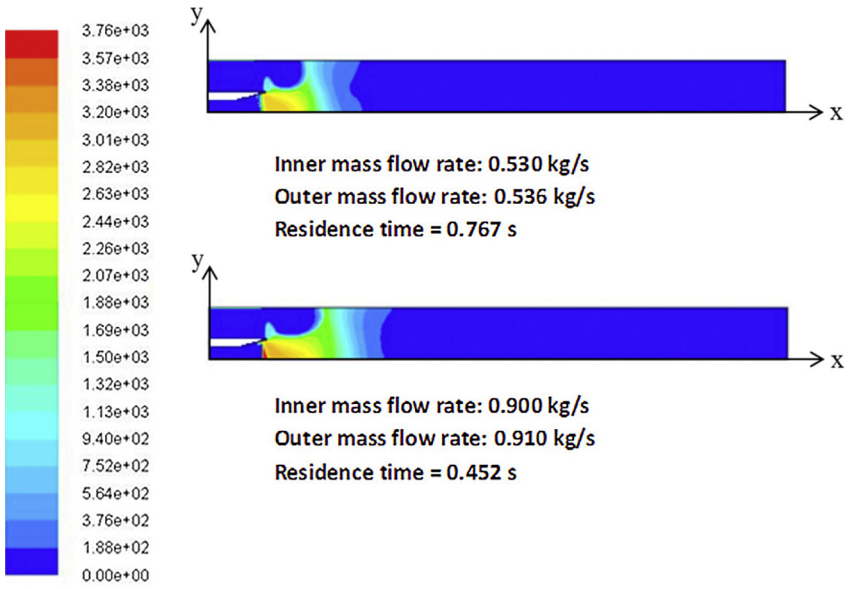

Fig. 15. Crystal growth rate G (μm/s) in the coaxial nozzle at steady state for different total mass input rates (outer inlet: methanol saturated with lovastatin, inner inlet: water, water to methanol ratio = 0.99). Upper boundary (outer wall). Lower boundary (nozzle axis). Nozzle radius = 0.01816 m, Nozzle length = 1.0 m.

some of the lowering of solubility by slightly increasing temperature in Environment 3. The maximum increase of temperature due to the mixing of methanol with water is 6.5 K, while that due to the heat of crystallization is 0.8 K.

As shown in Fig. 17, a higher maximum temperature occurs for the higher flow rate, which can be attributed to the greater delivery of solute, solvent and antisolvent per unit volume. In both cases, however, the region of maximum temperature is small. This results from the rapid turbulent dispersion of heat near this region which limits the effective temperature rise. At the point of initial mixing (X = 0.1 m), the heat of mixing increases the temperature of Environment 3 to just under 309 K. Further equilibration by mixing drops the temperature to 304 K at X = 0.2 m.

5.5. Effect of mass input rate on crystal size distribution

For three total mass input flow rates, all with an antisolvent to solvent flow ratio of 0.99, Figs. 18–22 show the cross-sectionally averaged crystal size distribution (CSD) at axial locations X = 0.12, 0.135, and 0.15 m, respectively, within the coaxial nozzle. The monotonically decreasing shape of the CSD resembles that of the simulations by Woo et al. [39] and also the experimental CSD of Mahajan and Kirwan [2] for an unconfined impinging jet. The lower the mass throughput, the longer is the residence time available for nucleation and crystal growth. Thus, CSD increases in breadth and magnitude as mass input rates decrease. Of course, crystal enlargement proceeds as the fluid mixture travels through the nozzle. As the axial location increases, the difference in CSD

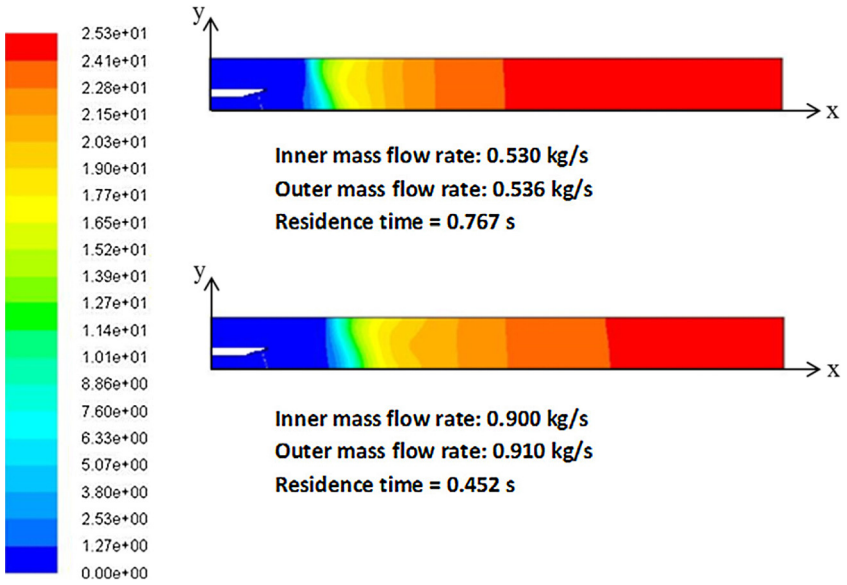

Fig. 16. Total mass density of crystals $\sum_{j=1}^{j=N_{cell}} f_{w,j}$ in the coaxial nozzle at steady state for different total mass input rates (outer inlet: methanol saturated with lovastatin, inner inlet: water, water to methanol ratio = 0.99). Upper boundary (outer wall). Lower boundary (nozzle axis). Nozzle radius = 0.01816 m, Nozzle length = 1.0 m.

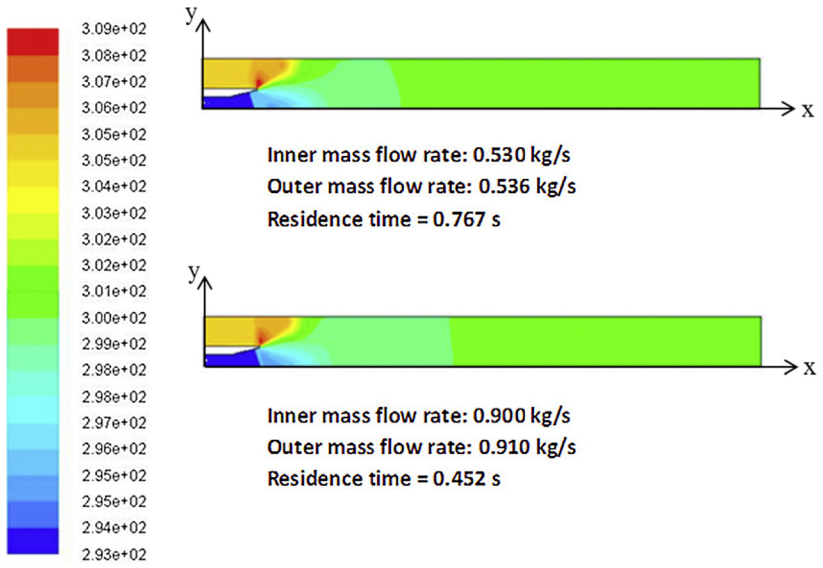

Fig. 17. Temperature T (K) in coaxial nozzle at steady state for different total mass input rates (outer inlet: methanol saturated with lovastatin, inner inlet: water, water to methanol ratio = 0.99). Upper boundary (outer wall). Lower boundary (nozzle axis). Nozzle radius = 0.01816 m, Nozzle length = 1.0 m.

with respect to input flow rate becomes less discernible, especially for lower crystal sizes.

Figs. 21 and 22 compare the crystal size distributions for various throughputs for fixed residence times of 0.01 and 0.02, respectively, which clearly show how an increase in residence time broadens the CSD. Also, even at the same residence time, the higher throughputs yield a sharper CSD, which agrees with experiments in unconfined impinging jets [2]. Table 4 shows that the percentage of solute converted to crystals declines only slightly with throughput, in spite of much lower residence times, which is due to the increased turbulent mixing of antisolvent with solvent.

6. Effect of mixer diameter upon crystallization

Turbulent transport properties could be affected by increasing the mixer diameter, all other conditions being equal. By holding input mass fluxes (in kg/m^2 s) constant and increasing the mixer diameter 10 and 20 percent from the base-case diameter 0.03632 m, calculations were made to determine the effect of the transverse dimensions on crystallization. That is, how adequate is transport in the radial direction. Table 5 shows the mixer parameters and the resulting crystallization percentage. Crystal size distributions corresponding to the three diameters are plotted in Figs. 23 and 24 for X = 0.12 m and X = 1.0 m, respectively.

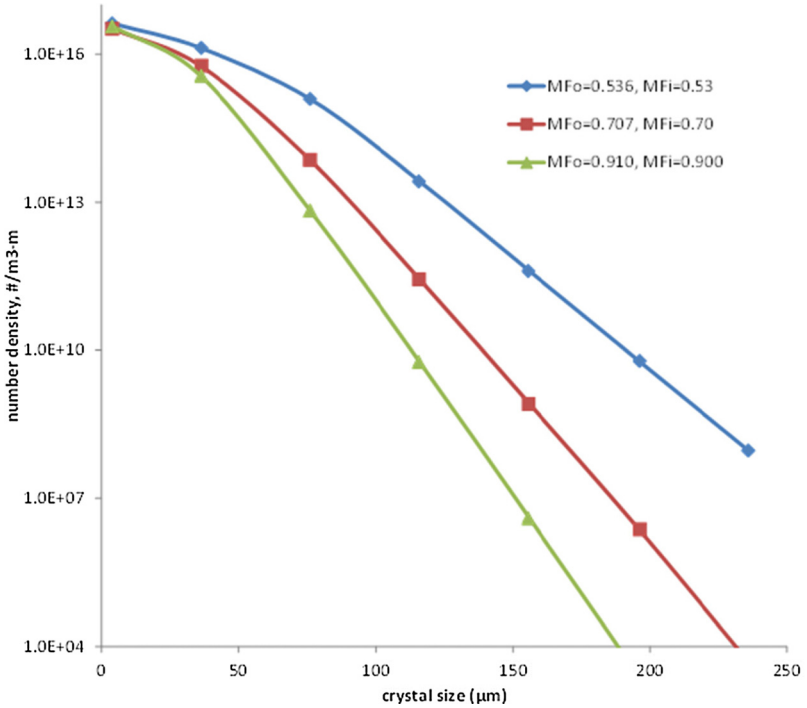

Fig. 18. Crystal size distribution at axial position X = 0.120 m for water (antisolvent) to methanol (solvent) flow ratio of 0.99 and various total mass flow rates.

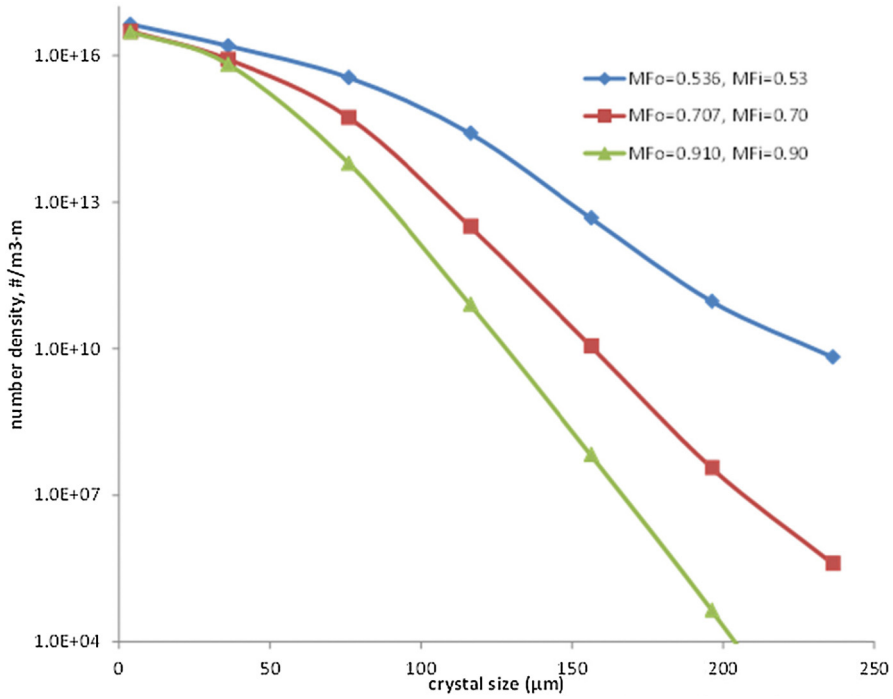

Fig. 19. Crystal size distribution at axial position $X = 0.135$ m for water (antisolvent) to methanol (solvent) flow ratio of 0.99 and various total mass flow rates.

Although there is some difference in CSD with respect to mixer diameter at $X = 0.12$ m, there is little difference at $X \geq 1.0$ m. For the flow conditions in Table 5, the results indicate that the turbulent transport parameters responsible for transport in the transverse direction are sufficiently high to overcome the effect of transport distances in the diameter range 3.6320–4.3584 cm.

7. Summary and conclusions

The results in this paper on the simulation of mixing and crystallization within a coaxial mixer are:

1. A simulation algorithm that couples macromixing and micromixing models with the solution to the full spatially-varying population balance equation (PBE) was implemented for a

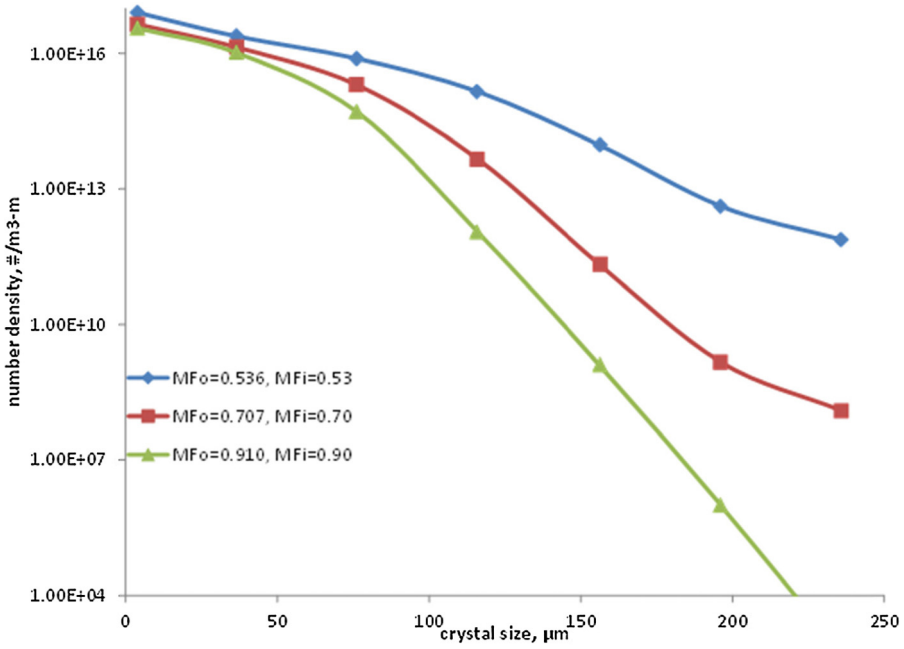

Fig. 20. Crystal size distribution at axial position $X = 0.150$ m for water (antisolvent) to methanol (solvent) flow ratio of 0.99 and various total mass flow rates.

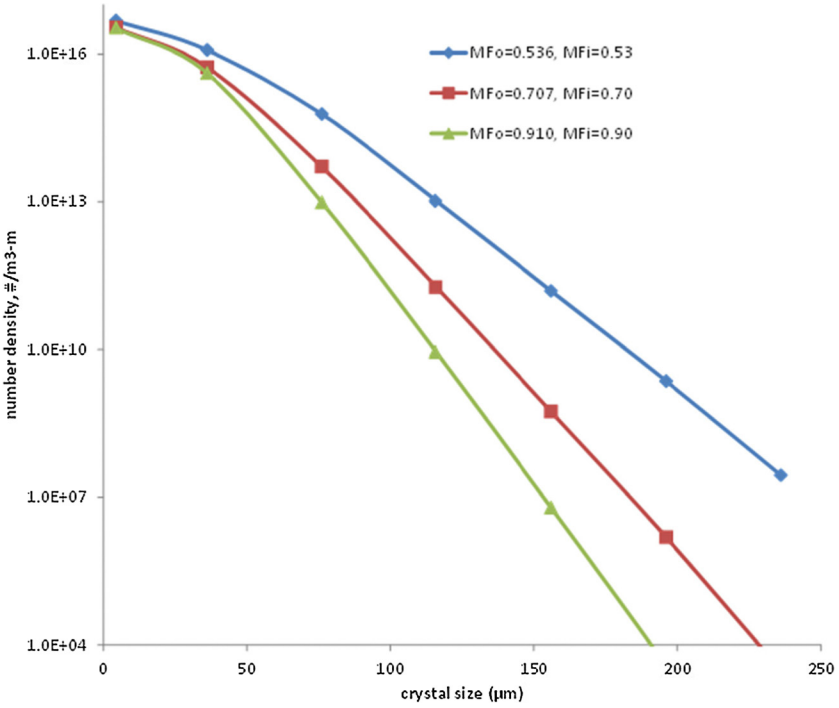

Fig. 21. Crystal size distribution at axial position τ_{res} = 0.01 s for water (antisolvent) to methanol (solvent) flow ratio of 0.99 and various total mass flow rates.

coaxial mixer via a Fluent user-defined function (UDF) file. The CFD-micromixing-PBE model computes the crystal size distribution throughout the crystallizer while taking into account the different mixing time and length scales. Crystal nucleation, growth, and dissolution kinetics were included in the model. An energy equation was incorporated to compute the temperature at every location and time in the mixer.

2. The UDF file was designed so that the user can readily replace the model parameters, including physical properties for antisolvent and solvent components. In the simulation results presented in this paper, the solvent was methanol and the antisolvent was liquid water.
3. Steady-state simulations were carried out by integrating the transient model equations until all of the variables converged to their steady-state values. Appropriate settings were found for the Fluent SETUP code that enabled stable and accurate calculations.
4. Simulation results were presented for the application of the CFD-micromixing-PBE code to antisolvent crystallization within

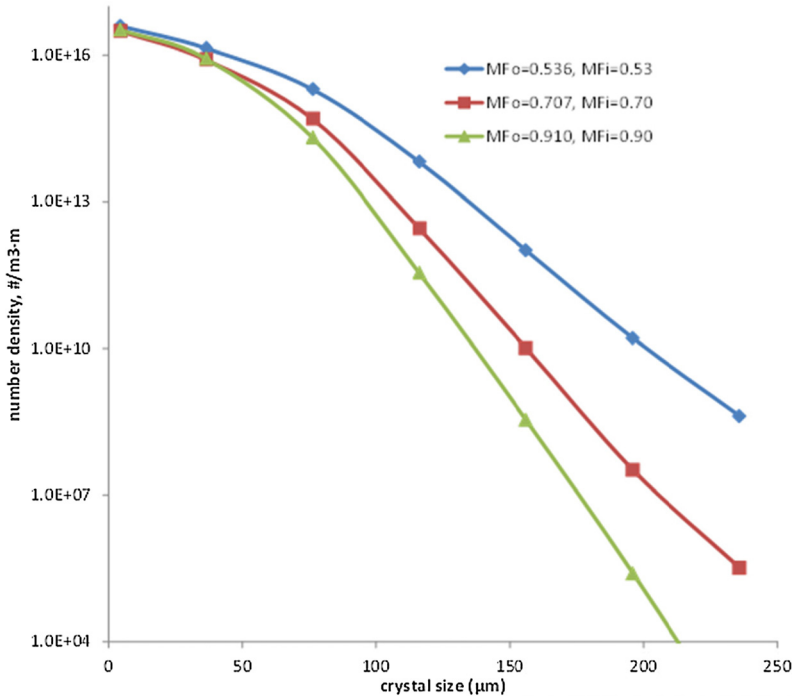

Fig. 22. Crystal size distribution at axial position τ_{res} = 0.02 s for water (antisolvent) to methanol (solvent) flow ratio of 0.99 and various total mass flow rates.

Table 5
Effect of mixer diameter on crystallization.

	Base diameter case	10% Larger diameter case	20% Larger diameter case
Mixer length, m	1	1	1
Mixer diameter, cm	3.6320	3.9952	4.3584
Annular mass flux, kg/m^2 s	829	829	829
Inner mass flux, kg/m^2 s	11626	11626	11626
Annular hydraulic diameter, m	0.021079	0.023186	0.025294
Inner hydraulic diameter, m	0.008756	0.009631	0.010507
Annular turbulent intensity, %	4.379	4.327	4.280
Inner turbulent intensity, %	3.787	3.742	3.702
Percentage solute Crystallized at X = 1.0 m	77.78	77.58	77.36

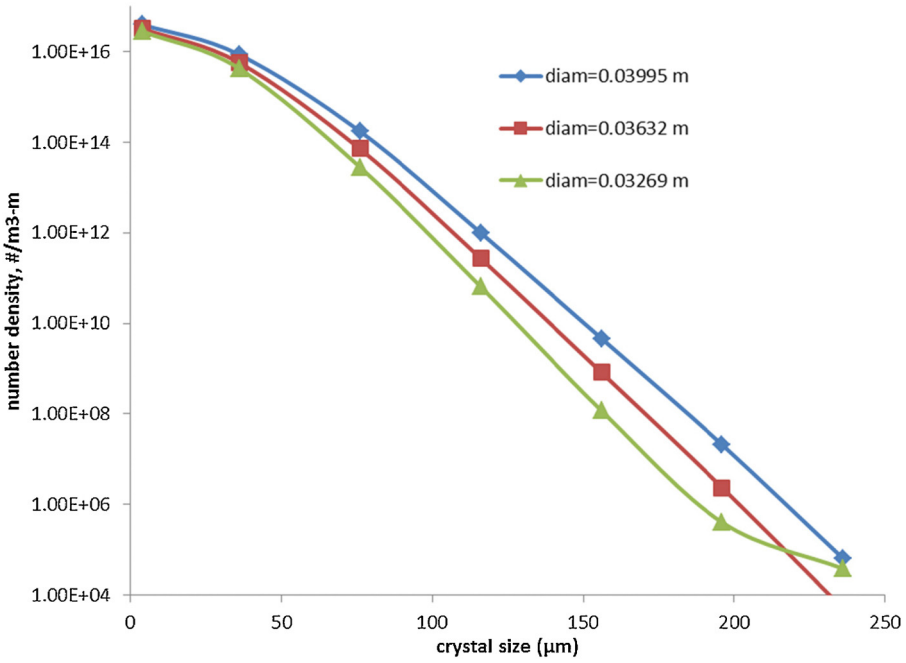

Fig. 23. Crystal size distribution at axial position X = 0.120 m for water (antisolvent) to methanol (solvent) flow ratio of 0.99, annular mass flux = 829 kg/m^2 s, inner mass flux = 11626 kg/m^2 s, and various mixing nozzle diameters.

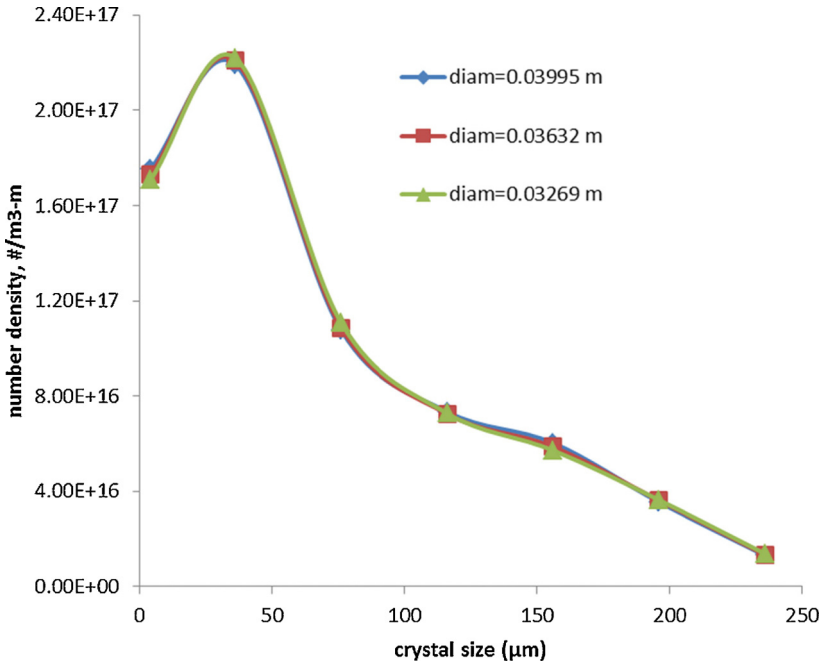

Fig. 24. Crystal size distribution at axial position X = 1.0 m for water (antisolvent) to methanol (solvent) flow ratio of 0.99, annular mass flux = 829 kg/m^2 s, inner mass flux = 11626 kg/m^2 s, and various mixing nozzle diameters.

a coaxial nozzle mixer. The model used solubility and crystallization kinetics for lovastatin that were available in the literature.
5. The simulations indicated the effect that operating conditions had upon total crystallization and crystal size distribution.

This detailed simulation of coaxial crystallizers parallels that done for impinging jet crystallizers. The results demonstrate the possibility of influencing crystal size distribution by adjusting operating conditions (such as inlet stream velocities) of the coaxial crystallizer. Such simulations can facilitate development in the pharmaceutical industry by providing a more insight into the crystallization process, and by reducing the number of experiments required to determine optimal operating conditions. This, in turn, reduces the quantity of active pharmaceutical ingredient (API) needed for the experiments. Consequently, the crystallizer process design can be performed much earlier during the drug development process, where a limited quantity of API is available.

Acknowledgements

Financial support from Pfizer, Inc. is acknowledged.

Appendix A.

Nomenclature

A_c Crystal surface area (m^2)

as_j	Concentration of antisolvent j in Environment 3 (kg/m_3^3)
b	Nucleation rate exponent
B	Nucleation rate (#/m^3 s)
c	Concentration of solute (kg/m^3 or kg/kg)
c^*	Solubility or saturation concentration (kg/m^3 or kg/kg)
Δc	Supersaturation (kg/m^3 or kg/kg)
c_i	Interfacial concentration (kg/m^3)
$C_{p,3}$	Specific heat of Environment 3, kJ/kg
C_μ	Constant in turbulent viscosity expression
D,D_m	Diffusion coefficient or laminar diffusivity (m^2/s)
d_p	Particle size (m_c)
D_t	Turbulent diffusivity (m^2/s)
f	Number density function (#/$m_c m^3$)
F	Target number density function (#/m)
f_r	Derivative of number density function (#/$m_c^2 m^3$)
f_w	Mass density function (kg/$m_c m^3$)
f_φ	Joint probability function of all scalars
g	Growth rate exponent
$\vec{g}$	Gravitational acceleration (m/s^2)
G	Growth rate (m/s)
$\boldsymbol{G}(\boldsymbol{p})$	Rate of change of $\boldsymbol{p} = (p_1\ p_2 \cdots p_{Ne})$ due to micromixing
$\boldsymbol{G}_s(\boldsymbol{p})$	Term to eliminate spurious dissipation rate in Eq. (12)
h	Enthalpy per unit volume, kJ/m^3
i	Exponent for solute integration
k	Turbulent kinetic energy (m^2/s^2) in turbulence and micromixing equations and Boltzmann's constant in nucleation rate expression
K	Tradeoff ratio between growth and nucleation rates ((μm/s)/(#/m^3 s))
k_1, k_2	Reaction rate constant (m^3/mol s)
k_b	Nucleation rate prefactor (#/m^3 s (kg/kg)^b)
k_a	Area shape factor
k_d	Mass transfer coefficient (m/s)
k_g	Growth rate prefactor (m/s (kg/kg)^g)
k_i	Integration rate constant (m^{3i-1}/kg^{i-1} s)
k_v	Volume shape factor
L	Crystal size (μm)
M^n	Rate of change of $\langle \mathbf{s} \rangle_n$ due to micromixing
$\mathbf{M}_s^n$	Term to eliminate spurious dissipation rate in Eq. (13)
m	Mass (kg)
$\dot{m}$	Mass flow rate (kg/s)
MW_{H_2O}	Molecular weight of water, kg/kmol
MW_{solute}	Molecular weight of solute, kg/kmol
N_A	Avogadro's number
N	Number of particle size cells or bins
N_e	Number of probability modes or environments
N_s	Total number of scalars (species)
p	Pressure (Pa) in momentum conservation equation
p_n	Probability of mode n or volume fraction of Environment n in micromixing model
r	Crystal size (m)
r_0	Nuclei size (m)
Δr	Discretized bin size for crystal size (m)
Re	Reynolds number
$\langle \mathbf{s} \rangle_n$	Weighted concentration of mean composition of scalars $\boldsymbol{\varphi}$ in mode n
S	Relative supersaturation = $\Delta c/c^*$
S_{as}	User-defined source term of antisolvent concentration (kg/m^3 s)
$S_{fw,j}$	User-defined source term of crystal mass density in the jth bin (kg/m_c m^3 s)
S_s	User-defined source term of solvent concentration (kg/m^3 s)
S_ε	User-defined source term for dissipation rate of turbulent kinetic energy
S_k	User-defined source term for turbulent kinetic energy
Sc	Schmidt number
Sc_t	Turbulent Schmidt number
Sh	Sherwood number
t	Time (s)
T	Temperature (°C)
t_I	Induction time (s)
t_M	Micromixing time (s)
t_s	Sampling time (s)
v	Molar volume in nucleation rate expression (m^3/mol)
V	Velocity vector (m/s)
V	Volume fraction of antisolvent
w	Antisolvent mass percent (%)
$\boldsymbol{x}$	Spatial position vector (m)
X	Reaction conversion
X_A	Fraction of polymorph A

Special units

m	Length unit (meter) in mixer/crystallizer
m_c	Length unit (meter) in crystal
m_3	Length unit (meter) in Environment 3

Symbols

α	Scalar
β	Geometric shape factor
Δc	supersaturation = $c - c^*$
ε	Turbulent kinetic energy dissipation rate (m^2/s^3)
ε_ξ	Scalar dissipation rate (1/s)
ϕ	Volume fraction of solids in an effective viscosity expression
ϕ_k	Scalar
$\langle \phi \rangle$	Mean composition of a scalar in an environment
ρ_3	Fluid density of Environment 3
γ	Interfacial tension [N/m]
λ_k	Kolmogoroff length scale
μ	Viscosity (kg/m s) effective viscosity of suspension (kg/m s) in effective viscosity expression

μ_n nth moment of number density function
μ_s Viscosity of suspending medium (kg/m s)
μ_t Viscosity (kg/m s)
θ Constant in minmod limiter
θ_j Parameter value
ρ Density (kg/m^3)
ρ_c Crystal density (kg/m^3)
σ_ε Turbulent Prandtl number for turbulent kinetic energy dissipation rate
σ_k Turbulent Prandtl number for turbulent kinetic energy
τ Stress tensor (kg/m s^2)
ν Kinematic viscosity (m^2/s)
$\langle\xi\rangle$ Mixture fraction
$\langle\xi'^2\rangle$ Mixture fraction variance
ψ A dummy variable
ψ_α An element of $\boldsymbol{\psi}$ corresponding to the scalar α

Subscripts
i Crystal dimension in population balance equation Instance for dropping seed crystals
c Denotes crystal property
j Discretized bin for crystal size in population balance equation
n Environment in micromixing model Order of moment

Appendix B.

High-Resolution, Finite-Volume, Semidiscrete Central Schemes

High-resolution finite-volume methods have been investigated primarily in the applied mathematics and computational physics literature [52]. These methods provide high accuracy for simulating hyperbolic conservation laws while reducing numerical diffusion and eliminating nonphysical oscillations that can occur with classical methods. Being in the class of finite volume methods, such methods are conservative, which ensures the accurate tracking of discontinuities and preserves the total mass within the computational domain subject to the applied boundary conditions. Another advantage is that these numerical schemes can be easily extended to solve multidimensional and variable-coefficient conservation laws.

High-resolution central schemes for nonlinear conservation laws, starting from the NT scheme of Nessyahu and Tadmor [62], have the advantages of retaining the simplicity of the Riemann-solver-free approach, while achieving at least second-order accuracy. Kurganov and Tadmor [63] and Kurganov et al. [64] extended the NT scheme to reduce numerical viscosity (nonphysical smoothing of the numerical solution) arising from discrete approximations of the advection term. This KT high-resolution finite-volume central scheme accumulates less dissipation for a fixed Δy as compared to the NT scheme, and can be used efficiently with small time steps since the numerical viscosity is independent of $(1/\Delta t)$. The limiting case, $\Delta t \to 0$, results in the second-order semidiscrete version. In addition, the KT method satisfies the scalar total-variation-diminishing (TVD) property with minmod reconstruction, which implies that the nonphysical oscillations that occur with many second-order accurate numerical methods cannot occur with this method. The KT semidiscrete scheme is particularly effective when combined with high-order ODE solvers for the time evolution.

Consider the nonlinear conservation law,

$$\frac{\partial}{\partial}u(y,t) + \frac{\partial}{\partial y}q(u(y,t)) = 0 \tag{B.1}$$

The semidiscrete central scheme of Kurganov and Tadmor [63] is classified as a finite-volume method, since it involves keeping track of the integral of u over each grid cell. The use of cell averages,

$$u_j(t) = \frac{1}{\Delta y}\int_{y_{j-1/2}}^{y_{j+1/2}} u(y,t)dy, \tag{B.2}$$

to represent computed values, where $\Delta y = y_{j+1/2} - y_{j-1/2}$, ensures that the numerical method is conservative. The second-order semidiscrete scheme admits the conservative form:

$$\frac{d}{dt}u_j(t) = -\frac{H_{j+1/2}(t) - H_{j-1/2}(t)}{\Delta y} \tag{B.3}$$

with the numerical flux

$$H_{j+1/2}(t) : = \frac{q(u^+_{j+1/2}(t)) + q(u^+_{j+1/2}(t))}{2} - \frac{a_{j+1/2}}{2}[u^+_{j+1/2}(t) - u^-_{j+1/2}(t)] \tag{B.4}$$

and the intermediate values given by

$$u^+_{j+1/2} := (u_{j+1/2}(t) - \frac{\Delta y}{2}(u_y)_{j+1}(t)$$
$$u^+_{j+1/2} := (u_j(t) - \frac{\Delta y}{2}(u_y)_j(t)$$

while the local propagation of speeds, for the scalar case, is

$$a_{j+1/2}(t) := \max_{u\in[u^-_{j+1/2}(t),u^+_{j+y2}(t)]} |q'(u^-_{j+1/2}(t))| \tag{B.6}$$

The derivatives are approximated with the minmod limiter:

$$(u_y)^n_j := \underset{1\le\theta\le2}{\text{minmond}}\left(\theta\frac{u^n_j - u^n_{j-1}}{\Delta y}, \frac{u^n_{j+1} - u^n_{j-1}}{2\Delta y}, \frac{u^n_{j+1} - u^n_j}{\Delta y}\right) \tag{B.7}$$

which is defined as

$$\text{minmond}(\alpha_1,\alpha_2,\ \ldots) = \begin{cases} \min\{\alpha_i\}_i & \text{if}\alpha_i > 0\forall i \\ \max\{\alpha_i\}_i & \text{if}\alpha_i > 0\forall i \\ 0 & \text{otherwise} \end{cases} \tag{B.8}$$

Selecting the value of $\theta = 1$ results in nonphysical smoothing of the numerical solution. A value of $\theta = 2$ results in minimal nonphysical smoothing, but can introduce some nonphysical oscillation. The value $\theta = 1.5$ is commonly selected to trade off minimizing the amount of nonphysical dissipation/smoothing with minimizing nonphysical oscillation. More details on such limiters can be found in the above References

References

[1] M.D. Lindrud, S. Kim, C. Wei, U.S. Patent #6302958, 2001.
[2] A.J. Mahajan, D.J. Kirwan, AIChE J. 42 (1996) 1801–1814.
[3] M. Midler, E.L. Paul, E.F. Whittington, M. Futran, P.D. Liu, J. Hsu, S.-H. Pan U.S. Patent #5314506, 1994.
[4] D.J. Am Ende, S.J. Brenek, Am. Pharm. Rev. 7 (2004) 98–104.
[5] S.S. Leung, B.E. Padden, E.J. Munson, D.J.W. Grant, J. Pharm. Sci. 87 (1998) 501–507.
[6] J.W. Mullin, Crystallization, Elsevier Butterworth-Heineman, Oxford, U.K, 2001.
[7] J.S. Wey, P.H. Karpinski, Batch crystallization, Handbook of Industrial Crystallization, Butterworth-Heinemann, Boston, 2002231–248.
[9] B.K. Johnson, R.K. Prud'homme, AIChE J. 49 (2003) 2264–2282.
[10] M. Fujiwara, Z.K. Nagy, J.W. Chew, R.D. Braatz, J. Process Control 15 (2005) 493–504.
[11] R. Dauer, J.E. Mokrauer, W.J. McKeel, U.S. Patent 5578279, 1996.
[12] M.D. Lindrud, S. Kim, C. Wei, U.S. Patent 6302958, 2001.
[13] D.J. Am Ende, T.C. Crawford, N.P. Weston, U.S. Patent 6558435, 2003.
[14] X. Wang, J.M. Gillian, D.J. Kirwan, Cryst. Growth Des. 6 (2006) 2214–2227.

[15] H. Wei, J. Garside, Chem. Eng. Res. Des. 75 (1995) 219–227.
[16] J. Baldyga, W. Orciuch, Chem. Eng. Sci. 56 (2001) 2435–2444.
[17] D.L. Marchisio, A.A. Barresi, M. Garbero, AIChE J. 48 (2001) 2039–2050.
[18] A.A. Öncül, K. Sundmacher, A. Seidel-Morgenstern, D. Thévenin, Chem. Eng. Sci. 61 (2006) 652–664.
[19] A. Borissova, Z. Dashova, X. Lai, K.J. Roberts, Cryst. Growth Des. 4 (2004) 1053–1060.
[20] J. Budz, P.H. Karpinski, J. Mydlarz, J. Nyvlt, Ind. Eng. Chem. Prod. Res. Dev. 25 (1986) 657–664.
[21] H. Charmolue, R.W. Rousseau, AIChE J. 37 (1991) 1121–1128.
[22] N. Doki, N. Kubota, M. Yokota, S. Kimura, S. Sasaki, J. Chem. Eng. Jpn. 35 (2002) 1099–1104.
[23] R.A. Granberg, D.G. Bloch, A.C. Rasmuson, J. Cryst. Growth 199 (1999) 1287–1293.
[24] X. Holmback, A.C. Rasmuson, J. Cryst. Growth 199 (1999) 780–788.
[25] S. Kaneko, Y. Yamagami, H. Tochihara, I. Hirasawa, J. Chem. Eng. Jpn. 35 (2002) 1219–1223.
[26] J.W. Mullin, N. Teodossiev, O. Sohnel, Chem. Eng. Process. 26 (1989) 93–99.
[27] J. Mydlarz, A.G. Jones, Powder Technol. 65 (1991) 187–194.
[28] J. Nyvlt, S. Zacek, Collect. Czech. Chem. Commun. 51 (1986) 1609–1617.
[29] E. Plasari, P. Grisoni, J. Villermaux, Chem. Eng. Res. Des. 75 (1997) 237–244.
[30] D.M. Shin, W.S. Kim, J. Chem. Eng. Jpn. 35 (2002) 1083–1090.
[31] H. Takiyama, T. Otsuhata, M. Matsuoka, Chem. Eng. Res. Des. 76 (1998) 809–814.
[32] Y. Kim, S. Haam, Y.G. Shul, W.S. Kim, J.K. Jung, H.C. Eun, K.K. Koo, Ind. Eng. Chem. Res. 42 (2003) 883–889.
[33] M. Kitamura, J. Cryst. Growth 237 (2002) 2205–2214.
[34] M. Kitamura, K. Nakamura, J. Chem. Eng. Jpn. 35 (2002) 1116–1122.
[35] M. Kitamura, M.J. Sugimoto, Cryst. Growth 257 (2003) 177–184.
[36] M. Okamoto, M. Hamano, H. Ooshima, J. Chem. Eng. Jpn. 37 (2004) 95–101.
[37] J.W. Schroer, K.M. Ng, Ind. Eng. Chem. Res. 42 (2003) 2230–2244.
[38] X.Y. Woo, R.B.H. Tan, P.S. Chow, R.D. Braatz, Cryst. Growth Des. 6 (2006) 1291–1303.
[39] X.Y. Woo, Modeling and simulation of antisolvent crystallization: mixing and control, Ph.D. Thesis, University of Illinois, Urbana-Champaign, 2007.
[40] X.Y. Woo, R.B.H. Tan, R.D. Braatz, Cryst. Growth Des. 9 (2009) 156–164.
[41] R.O. Fox, Computational Models for Turbulent Reacting Flows, Cambridge University Press, Cambridge, U.K, 2003.
[42] A. Varma, M. Morbidelli, H. Wu, Parametric Sensitivity in Chemical Systems, Cambridge University Press, Cambridge, U.K, 1999.
[43] A.J. Mahajan, D.J. Kirwan, J. Cryst. Growth 144 (1994) 281–290.
[44] S.B. Pope, Turbulent Flows, Cambridge University Press, Cambridge, U.K, 2000.
[45] Fluent User's Guide, ANSYS Fluent User's Guide, Release 14.0. ANSYS, Inc., Canonsburg, Pennsylvania, 2011.
[46] Ansys 14.5, www.ansys.com/Products/ANSYS 14.5 Release Highlights.
[47] H.M. Hulburt, S. Katz, Chem. Eng. Sci. 19 (1964) 555–574.
[48] A.D. Randolph, M.A. Larson, Theory of Particulate Processes, Academic Press, Inc., San Diego, California, 1988.
[49] R. Gunawan, I. Fusman, R.D. Braatz, AIChE J. 50 (2004) 2738–2749.
[50] D.L. Ma, R.D. Braatz, D.K. Tafti, Int. J. Mod. Phys. B 16 (2002) 383–390.
[51] D.L. Ma, D.K. Tafti, R.D. Braatz, Ind. Eng. Chem. Res. 41 (2002) 6217–6223.
[52] D.L. Ma, D.K. Tafti, R.D. Braatz, Comput. Chem. Eng. 26 (2002) 1103–1116.
[53] R.J. Leveque, Finite Volume Methods for Hyperbolic Problems, Cambridge University Press, Cambridge, U.K, 2002.
[54] L.G. Wang, R.O. Fox, AIChE J. 50 (2004) 2217–2232.
[55] D.L. Marchisio, A.A. Barresi, R.O. Fox, AIChE J. 47 (2001) 664–676.
[56] D.L. Marchisio, R.O. Fox, A.A. Barresi, G. Baldi, Ind. Eng. Chem. Res. 40 (2001) 5132–5139.
[57] D.L. Marchisio, R.O. Fox, A.A. Barresi, M. Garbero, G. Baldi, Chem. Eng. Res. Des. 79 (2001) 998–1004.
[58] D. Piton, R.O. Fox, B. Marcant, Can. J. Chem. Eng. 78 (2000) 983–993.
[59] G.L. Bertrand, F.J. Millero, C.-H. Wu, L.G. Hepler, J. Phys. Chem. 70 (1966) 699–705.
[60] H.H. Tung, E.L. Paul, M. Midler, J.A. McCauley, Crystallization of Organic Compounds: An Industrial Perspective, John Wiley & Sons, Hoboken, New Jersey, 2009.
[61] H. Sun, J.-B. Gong, J.-K. Wang, J. Chem. Eng. Data 56 (2006) 1389–1391.
[62] A.J. Mahajan, D.J. Kirwan, AIChE J. 42 (1996) 1801–1814.
[63] H. Nessyahu, E. Tadmor, J. Comput. Phys. 87 (1990) 408–463.
[64] A. Kurganov, E. Tadmor, J. Comput. Phys. 160 (2000) 241–282.
[65] A. Kurganov, S. Noelle, G. Petrova, SIAM J. Sci. Comput. 23 (2001) 707–740.
[66] Y. Liu, R.O. Fox, AIChE J. 52 (2006) 731–744.